



**Arab American University**

**Faculty of Graduate Studies**

**CdSe based electro-optical systems designed for optoelectronic applications**

By

**Heyam Hashim Awad Ghannam**

Supervisor

**Prof. Dr. Atef Fayez Qasrawi**

**This Thesis was submitted in partial fulfillment of the requirements for the  
Master's degree in Physics**

**July/2024**

**© Arab American University- 2024. All rights reserved.**

## Thesis Approval

**CdSe based electro-optical systems designed for optoelectronic applications**

By

**Heyam Hashim Awad Ghannam**

This thesis was defended successfully on July 9<sup>th</sup> 2024 and approved by:

Committee members

Signature

1. Prof. Dr. Atef Fayez Qasrawi: Supervisor
2. Prof. Dr. Hazem Khanfar: Internal Examiner
3. Assoc. prof. Dr. Iyad Saadeddin: External Examiner



## **Declaration**

The work provided in this thesis, unless otherwise referenced, is the researcher's own work, and has not been submitted elsewhere for any other degree or qualification.

Student's Name: Heyam Hashim Awad Ghannam

Student ID: 202120195

Signature: Heyam Ghannam

Date: November 13<sup>th</sup> 2024

## **Acknowledgment**

In the name of God, the Most Gracious, the Most Merciful, who alone is responsible for my success.

Thank God, I've finished my master's thesis at my esteemed institution, Arab American University. I credit my triumph to myself first, and then to everyone who has given me unrestricted support and without payment. Specifically, the honorable Professor Dr. Atef Qasrawi, who has spared no effort in order for the thesis to see the light, was one of the people who supported me in getting here. God rewarded him with the best reward. And for all my virtuous doctors in general.

To those who make my eyes happy to see their faces, to my mother and father, who never stopped believing in me. To my parents, who gave me the gift of dreams and the ability to realize them. If it weren't for all your efforts and faith in me, I wouldn't have been here. I always thank God for being by my side.

To those whose faces light up my eyes when I meet them, to those who share my moments and triumphs and who are as joyful about them as if they were my brothers and sisters. I'm grateful.

For the friends who became family, the friends who believed in me when I didn't, and for those rare, beautiful friendships that change our lives forever. Thank you.

## Abstract

In this thesis we aimed to enhance the optical properties of CdSe thin films by coating it onto a highly conductive SiO<sub>2</sub> substrates. Thin films of CdSe are coated by the thermal evaporation techniques onto conductive SiO<sub>2</sub> substrates under a vacuum pressure of 10<sup>-4</sup> mbar. Stacked layers of SiO<sub>2</sub> films comprising Au nanosheets (SAS) are used. It is observed that SiO<sub>2</sub> substrates containing Au nanosheets in its structure significantly modulate the structural and optical properties of CdSe. Namely, the lattice constants of hexagonal CdSe decreased upon replacement of glass by SAS substrates. The micro strain, stacking fault percentage and defect density also decreased indicating the enhanced crystallinity of the films by SAS substrates. In addition it is observed that SAS films don't play a significant role on the energy band gap, but forms energy tails in the band gap. The exponential tail states narrow as the thickness of Au layer increases. On the other hand, the dielectric dispersion analyses have shown that the dielectric constant spectra are determined by three oscillators which blue-shifts upon replacement of glass by SAS substrates. The dielectric constant values decreased with increasing Au layer thickness in the substrate owing to the free charge density resulting from a thicker Au layer. On the other hand, the optical conductivity spectra which were modeled using Drude-Lorentz approach showed interesting features. Particularly, the optical conductivity of CdSe increased and the free carrier density increased after using SAS substrates. These features make the films under study more adequate for optoelectronic applications.

**Table of Contents**

Title	Page No.
Thesis Approval	I
Declaration	II
Acknowledgment	III
Abstract	IV
List of Tables	VIII
List of Figures	IX
List of Definitions of Abbreviations	XII
Chapter One Introduction	1
Chapter Two Theoretical Background	3
2.1 The X-ray diffraction	3
2.1.1 Bragg's law	4
2.1.2 Structural parameters	5
2.1.3 Crystallography	6
2.2 Optical properties	7
2.2.1 Absorption of light in matter	8

2.2.2 Tauc's equation and band gap measuring	10
2.2.3 Direct and indirect transitions	10
2.2.4 Band tails	11
2.2.5 Dielectric constant spectra	12
2.2.6 Drude-Lorentz model	17
Chapter Three Experimental Details	20
3.1 Glass cleaning	20
3.2 Thin films preparation	20
3.3 Thin films analysis	23
3.3.1 The Hot-Probe technique	24
3.3.2 The X-ray Diffraction (XRD) measurements	25
3.3.3 The optical measurements	26
3.3.4 The morphological measurements	27
Chapter Four Results and Discussion	28
4.1 Structural analysis	28
4.2 Morphological analysis	33

4.3 Optical analysis	36
4.4 Dielectric analysis	43
Chapter Five Conclusion	51
References	52
المخلص	62

---

**List of Tables**

No	Title	Page No.
2. 1	The seven lattice groups in three dimensions.	7
4. 1	The structural parameters of the main peak of CdSe, SAS-00/CdSe, SAS-100/CdSe and SAS-200/CdSe.	31
4. 2	The ionic radius of Cd, Se, Si, O and Au atoms.	32
4. 3	The bond length and the bond energy of the bonding atoms.	32
4. 4	The electronic configuration of Cd, Se, Si, O and Au atoms.	32
4. 5	The optical conduction parameters for (a) CdSe, (b) SAS-00/CdSe, (c) SAS-100/CdSe, (d) SAS-200/CdSe	48

## List of Figures

No	Caption	Page No.
2.1	The schematic diagram of the X-ray diffractometer.	3
2.2	The schematic diagram of Bragg scattering on the lattice surface.	4
2.3	The (a) direct and (b) indirect band gap transitions.	11
3.1	The (a) ion coater sputtering machine (b) schematic diagram of the ion coater sputtering machine.	21
3.2	The 600 VCM evaporation system.	22
3.3	The optical images of the real films of (a) CdSe, (b) SAS-00/ CdSe, (c) SAS-100/CdSe and (d) SAS-200/CdSe films.	22
3.4	The geometrical design of the real films of (a) CdSe, (b) SAS-00/ CdSe, (c) SAS-100/CdSe and (d) SAS-200/CdSe films.	23
3.5	The set-up of hot-probe technique.	24
3.6	X-ray Rigaku diffractometer.	25
3.7	The UV-VIS spectrophotometer.	26
3.8	The Scanning Electron Microscopy.	27
4.1	The X-ray diffraction patterns for standard card, CdSe, SAS-00/CdSe, SAS-100/CdSe and SAS-200/CdSe films.	28

Inset.1 shows the shift in the XRD main peak.

- |     |  |    |
|-----|--|----|
| 4.2 | SEM image for sample (a) SAS-00/CdSe for 54 enlargement,<br><br>(b, c) SAS-00/CdSe for 1K enlargement in different sites, and<br><br>(d) SAS-00/CdSe for 2.3 K Enlargements. | 34 |
| 4.3 | SEM image for sample (a) CdSe, (b) SAS-00/CdSe, (c) SAS-100/CdSe,<br><br>and (d) SAS-200/CdSe for 10K enlargement and recorded at 25 KV.                                     | 35 |
| 4.4 | The transmittance of CdSe, SAS-00/CdSe, SAS-100/CdSe,<br><br>and SAS-200/CdSe films.   | 37 |
| 4.5 | The reflectance of CdSe, SAS-00/CdSe, SAS-100/CdSe,<br><br>and SAS-200/CdSe films.   | 38 |
| 4.6 | The absorption coefficient spectra of CdSe, SAS-00/CdSe, SAS-100/<br><br>CdSe, and SAS-200/CdSe films.   | 40 |
| 4.7 | The $\ln(\alpha)$ -E variation in the low absorption region for band tail<br><br>investigation CdSe, SAS-00/CdSe, SAS-100/CdSe, and SAS-200<br><br>/CdSe films.              | 40 |
| 4.8 | The $(\alpha E)^{2/3}$ -E in the strong absorption region for CdSe, SAS-00/<br><br>CdSe, SAS-100/CdSe and SAS-200/CdSe.  | 41 |
| 4.9 | The $(\alpha E)^{2/3}$ -E in the weak absorption region for SAS-200/CdSe   | 42 |

in the low energy region.

- |      |   |    |
|------|---|----|
| 4.10 | The light absorbability for SAS-00/CdSe, SAS-100/CdSe and SAS-200/CdSe.   | 43 |
| 4.11 | The real part of the dielectric spectra for (a) SAS-00/CdSe, SAS-100/CdSe and CdSe films (b) SAS-200/CdSe.  | 44 |
| 4.12 | The imaginary part of the dielectric spectra for CdSe, SAS-00 /CdSe, SAS-100/CdSe and SAS-200/CdSe films.   | 45 |
| 4.13 | The optical conductivity for CdSe, SAS-00/CdSe, SAS-100/CdSe and SAS-200/CdSe films.  | 46 |
| 4.14 | The imaginary part of the dielectric constant spectra fitted according to the Drude-Lorentz model for (a) CdSe, (b) SAS-00/CdSe, (c) SAS-100/CdSe and (d) SAS-200/CdSe. | 47 |
-

**List of Definitions of Abbreviations**

---

Symbol	Symbol Meaning
CdSe	Cadmium selenide
SiO <sub>2</sub>	Silicon Oxide
$\lambda$	Wavelength
d	Inter-planner distance
$\theta$	Bragg angle
n	Integer
hkl	Miller indices
D	Crystallite size
$\beta$	Full width of the peak at half maximum (FWHM) measured in radians
$\varepsilon$	Lattice strain
$\delta$	Dislocation density
SF %	Stacking faults
E <sub>g</sub>	Energy band gap
$\alpha$	Absorption coefficient
T	Transmittance

---

R	Reflectance
A	Absorbance
$E_0$	The width of the band tails
$\vec{E}$	The electric field
$\vec{H}$	The magnetic field
$\vec{J}$	The current density
$\vec{D}$	The electric fields in the medium
$\vec{B}$	The magnetic fields in the medium
$\varepsilon$	The dielectric constant
$\mu$	The complex magnetic permeability
$\sigma$	The complex electrical conductivity
$\vec{K}$	The complex propagation constant
$\omega$	The light's frequency
$\varepsilon_r$	The real part of the dielectric constant
$\varepsilon_{im}$	The imaginary part of the dielectric constant
$\varepsilon_{eff}$	The effective dielectric constant

$c$	The speed of electromagnetic wave in free space
$\tilde{k}$	The imaginary part of the complex refractive index
$\tilde{n}$	The real part of the complex refractive index
$m_0$	The electron mass

---

## Chapter One

### Introduction

To bring technical comforts to contemporary society, new-generation electronics must be developed toward lighter, thinner, multifunctional, and cheaper electronic products. For the majority of thin-film electronics, transparent conductive films (TCFs) are essential materials because they combine strong electrical conductance with optical transparency. They are an essential part of many optoelectronic devices, such as photo detectors, sensors, e-skins, solar cells, laptops, displays, mobile phones and smart windows [1]. In this study, we will focus on CdSe thin film because of its good absorbance in the visible light spectrum [2]. It is important and interesting for its applications, which include optoelectronics device, photoconductors [3], thin film transistors [4], solar cells [5, 6], photographic photoreceptors [7], gas sensors [8], acousto-optic devices [9], etc.

Various methods have been used to prepare CdSe thin films, such as metal oxide molecular beam epitaxy [10], molecular beam epitaxy [11], Laser ablation techniques [12], chemical bath deposition, vacuum evaporation [13] and hot wall deposition technique [14]. Additionally in physical vapor deposition, thermal evaporation technique was also used to prepare CdSe thin films [15].

CdSe exhibits interesting structural properties, as explored by the X-ray diffraction technique. Particularly, CdSe has two crystal structures: the cubic zinc blende crystal structure and the hexagonal wurtzite structure [16]. However, hexagonal phase has a reflection plane oriented along (0 0 2) direction with lattice parameters of  $a = b = 4.425 \text{ \AA}$  and  $c = 6.934 \text{ \AA}$  [17]. On the

other hand, cubic structure has a reflection plane oriented along (1 1 1) direction [18] with a lattice parameter of  $a = 6.077 \text{ \AA}$  [17]. In addition, based on the preferred crystal structure Cadmium selenide (CdSe) has a direct optical band gap of  $\sim 1.79 \text{ eV}$  in the wurtzite crystal phase and  $\sim 1.71 \text{ eV}$  in the zinc blende phase [19].

After learning about some properties of CdSe thin films from other studies, we made the decision to investigate this film in this thesis. These studies covered optical, structural, and dielectric topics, which facilitated their rapid growth and widespread application in a range of products and industries, including solar cells [5, 6], biosensors, opto-electronic devices [3], light-emitting diodes (LEDs) and field-effect transistors (FETs) [20].

The work here will focus on the role of electro-optical windows on the performance of CdSe as a future promising member in optoelectronics. The enhancements in the light absorbability and optical conductivity will be a main target of the work. The study will include growing CdSe thin films and coating them with electro-optical windows. The properties of these optoelectronic components will be explored by means of standard techniques available in the physics laboratories. Some practical applications including the photo response of the device will be considered. Chapter two of this thesis will discuss some of the theoretical considerations required to explain the experimental results. We will demonstrate the experimental methods used to create and examine the prepared films in the third chapter. Fourth chapter presents the achieved results, explanations, and discussions of the observations.

## Chapter Two

### Theoretical Background

#### 2.1 The X-ray diffraction

In materials science, X-ray diffraction is a useful nondestructive method for identifying whether crystallographic order exists in solid state materials or not. This method can be used to determine whether a solid substance is crystalline or amorphous [21]. As shown in Fig. 2.1, basically, the XRD device consists of the X-ray source, a sample stage, and the X-ray detector. In this figure, the angle  $\theta$  is located between the plane of the sample and the X-ray source. Additionally, the angle  $2\theta$  is placed between the X-ray source and the detector. The incident beam of monochromatic X-rays is scattered by each atom inside the sample.

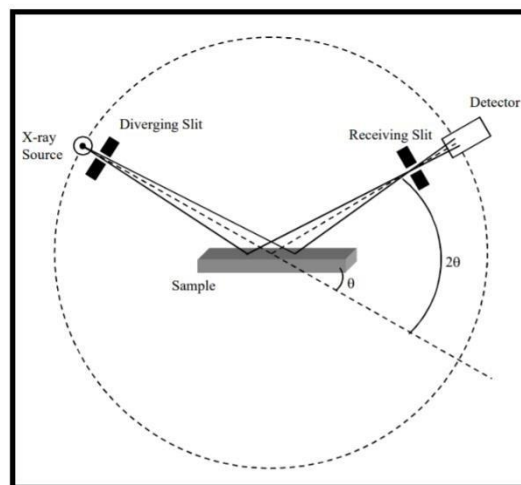


Fig. 2.1 The schematic diagram of the X-ray diffractometer.

### 2.1.1 Bragg's law

Bragg's law is the basis of X-ray diffraction analysis. It indicates that all of the rays scattered from atoms are at the same locations on parallel planes spaced  $d$  apart. After the irradiation is incident on the sample, constructive interference of the radiation from successive planes occurs when the path difference is an integer number  $n$  of wavelengths  $\lambda$ . Under constructive interference, Bragg's law is defined as [22]

$$2 d \sin \theta = n \lambda \quad (2.1)$$

Where  $d$  is the interplanar distance between two plans of atoms, which is measured in angstrom,  $\theta$  is the angle between the incident beam and the plane surface, the integer  $n$  is the order of the corresponding reflection, and  $\lambda$  is the wavelength of the incident X-ray beam, which is equal to  $1.5405 \text{ \AA}$  for copper  $K\alpha$  anode.

According to Bragg's law, constructive interference happens when the path difference between the two waves is equal to multiple integers of the wavelengths [23].

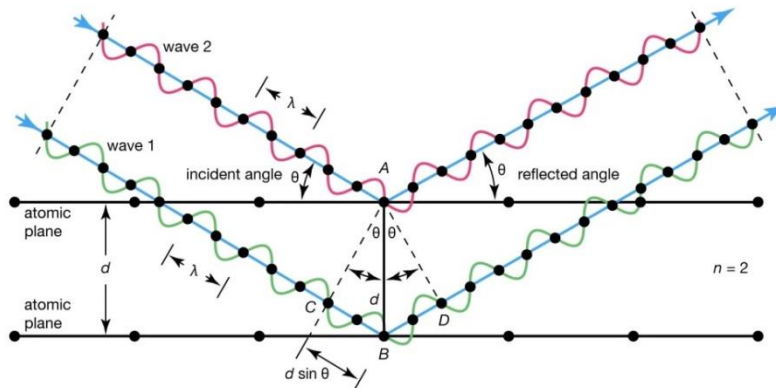


Fig. 2.2 The schematic diagram of Bragg scattering on the lattice surface.

If the interplanar distance is assumed to be known, the quadratic equations reveal the lattice parameters of the individual lattice planes with indices  $h$ ,  $k$ ,  $l$  for the cubic crystal systems defined as [24],

$$\frac{1}{d_{hkl}^2} = \frac{(h^2+k^2+l^2)}{a^2} \quad (2.2)$$

Where,  $a$  and  $c$  is the lattice constant along the  $a$  and  $c$  axis, respectively.

### 2.1.2: Structural parameters

Different structural parameters were measured by using the XRD pattern study. Some of these parameters are grain size ( $D$ ), lattice strain ( $\epsilon$ ), dislocation density ( $\delta$ ), and stacking faults ( $SF$  %). These parameters are determined from the broadening width  $\beta$  of the most intensive peak by the following relations [25, 26].

Strain ( $\epsilon$ ): is the ratio of contraction or expansion in bond lengths to the original bonds' lengths [26].

$$\epsilon = \frac{\beta}{4 \tan \theta} \quad (2.3)$$

"Crystallite" size ( $D$ ): is the diameter of an individual "Crystallite" in the crystal [26].

$$D = \frac{0.94\lambda}{\beta \cos \theta} \quad (2.4)$$

Dislocation density ( $\delta$ ): is a measure of the number of dislocations in a unit volume of crystalline material [26]. Measured in (lines/cm<sup>2</sup>)

$$\delta = \frac{15\epsilon}{aD} \quad (2.5)$$

Where  $\varepsilon$  is the strain,  $D$  is the crystallite size, and  $a$  is the lattice constant along the a- axis.

Stacking faults (SF %): are two dimensional planar defects that can occur in crystalline materials [26].

$$SF\% = \frac{2\pi^2\beta}{45\sqrt{3}\tan\theta} \times 100\% \quad (2.6)$$

### 2.1.3 Crystallography

The crystals are a periodic array of identical construction blocks arranged in three dimensions. A unit cell is the smallest volume element that characterizes the crystals. The atoms in crystalline materials are arranged in planes separated by a distance  $d$ . The dimensions of the unit cells (Size and shape) are described by the length of three axes ( $a$ ,  $b$ , and  $c$ ) with  $\alpha$ ,  $\beta$ , and  $\gamma$  angles between them [27].

In three-dimensional arrangements, there are seven groups or families of crystals, which are further split into fourteen different configurations of crystal lattices. These configurations are known as Bravais lattices [28]. Axes length, angle between axes, and symmetry characteristics are used to classify these Bravais lattices [27]. Table 2.1 represents the seven groups of the main Bravais lattice.

Table 2.1 The seven lattice groups in three dimensions.

System	Number of lattices	Restrictions on conventional cell axes and angles
Triclinic	1	$a \neq b \neq c, \alpha \neq \beta \neq \gamma \neq 90^\circ$
Monoclinic	2	$a \neq b \neq c, \alpha = \beta = 90^\circ \neq \gamma$
Orthorhombic	4	$a \neq b \neq c, \alpha = \beta = \gamma = 90^\circ$
Tetragonal	2	$a = b \neq c, \alpha = \beta = \gamma = 90^\circ$
Cubic	3	$a = b = c, \alpha = \beta = \gamma = 90^\circ$
Hexagonal	1	$a = b \neq c, \alpha = \beta = 90^\circ, \gamma = 120^\circ$
Trigonal	1	$a = b = c, \alpha = \beta = \gamma$

## 2.2 Optical properties

The wide variety of optical properties of the semiconductor materials makes them promising in opto-electronic applications. An ordinary classification of optical processes entails reflection, absorption, and transmission. Imagine a light beam traveling from a vacuum into a medium at a given propagation thickness. The incident beam can either travel through until it reaches the back surface or be reflected off the front surface. It is possible for the light on the back surface to be transmitted or reflected outside the medium. There are four processes for linear optical propagation. These mechanisms include scattering, refraction, absorption, and luminescence [29].

Refraction can be referred to as light bending when it passes from one interface to another due to the reduction of the light velocity when it propagates through the medium. This phenomenon is described by Snell's law as [29].

$$n_1 \sin \theta_1 = n_2 \sin \theta_2 \quad (2.7)$$

In essence, absorption has to do with how light frequency propagates. Light will be absorbed when its frequency matches that of the natural frequency of a solid substance.

Transmittance ( $T$ ), reflectance ( $R$ ), absorption coefficient ( $\alpha$ ), energy band gap ( $E_g$ ), and dielectric constant ( $\epsilon$ ) are all measured as part of the study of optical characteristics.

### 2.2.1 The absorption coefficient

One of the most common techniques to gain information about the band structure and energy gap ( $E_g$ ) of semiconductor materials is the analysis of optical absorption spectra. Absorption is concerned with photon-electron interactions. If the photon is absorbed inside the material, it will be able to excite an electron and transfer it from the valence band to the conduction band. The material's light absorption is expressed by the absorption coefficient ( $\alpha$ ), which is the rate at which incident light intensity is attenuated over the propagated distance.

Since the photon momentum ( $\frac{h}{\lambda}$ ) is less than the crystal momentum ( $\frac{h}{a}$ ), electron momentum is maintained conservatively even when the photon is absorbed.

The transmittance of light in the case of two parallel surfaces is obtained by the following expression [30],

$$T = (1 - R_1)(1 - R_2)e^{-\alpha d} \quad (2.8)$$

Where  $R_1$  and  $R_2$  represent the reflectivity of the front and back film surface and  $d$  is the medium thickness. If  $R_1 = R_2$ , equation (2.8) become [26],

$$T = (1 - R)^2 e^{-\alpha d} \quad (2.9)$$

When depositing three materials onto a glass substrate, the term  $(1 - R_3)$  should be added in the equation (2.8).

One way to express the multilayer film's transmittance is as follows:

$$T = \frac{(1-R_1)(1-R_2)e^{-\alpha d}}{1-R_1R_2e^{-2\alpha d}} \quad (2.10)$$

The absorbance ( $A$ ) of a grown film can be calculated if the transmittance ( $T$ ) and reflectance ( $R$ ) of the film are known:

$$A = -\ln\left(\frac{T}{(1-R_{glass})(1-R_{sample})}\right) \quad (2.11)$$

If the thickness of the film ( $d$ ) is monitored, the absorption  $\alpha$  ( $h\nu$ ) can be connected to the absorbance ( $A$ ) of the film using the following relation:

$$A = \alpha d \quad (2.12)$$

Thus, the absorption coefficient  $\alpha$  ( $h\nu$ ) at thickness  $d$  is written as [29]:

$$\alpha = \frac{-\ln\left(\frac{T}{(1-R_{glass})(1-R_{sample})}\right)}{d} \quad (2.13)$$

### 2.2.2 Tauc's equation and band gap measuring:

The energy gap is specified by using the spectrophotometric absorption spectrum in order to understand and get more predictive information about solids characteristics. Therefore, Tauc's equation, which links the incident photon energy with the spectrophotometric absorption coefficient, is applied. This equation indicates that the energy band gap is directly proportional to  $(\alpha E)^{1/p}$  as specified in the following equation [31, 32],

$$(\alpha E)^{1/p} = B(E - E_g) \quad (2.14)$$

Where  $E$  is the incident photon (light) energy,  $B$  is a constant that principally depends on the transition probability of electrons,  $E_g$  represents the energy gap, and  $p$  is an index that determines the type of the optical absorption process.

$p$  can have the values 2, 1/2, 3, and 3/2 corresponding to indirect allowed, direct allowed, indirect forbidden, and direct forbidden electronic transitions, respectively [33].

Plotting  $(\alpha E)^{1/p}$  against the incident photon energy  $E$  can be used to determine the material  $E_g$  taking the widest range of linear data in the high absorption region upon linear fitting, and the energy gap for semiconductor materials can be determined from the intercept with the  $E - axis$ .

### 2.2.3 Direct and indirect transition:

The band gap energy is the energy range between the valence band and conduction band where the electron states are forbidden inside them. The top of the valence band and the bottom of the

conduction band appear to have the same momentum value in the direct band gap. In contrast, the indirect band gap is characterized by the maximum of the valence band and the minimum of the conduction band being dissimilar in momentum value (k-vectors). This difference in k-vectors exhibits misaligned bands that require phonon assistance for excited electrons to be absorbed into the conduction band. However, no phonon assist is required, and there is no change in the crystal momentum (k) for the direct band gap materials [34]. As illustrated in Fig.2.3.

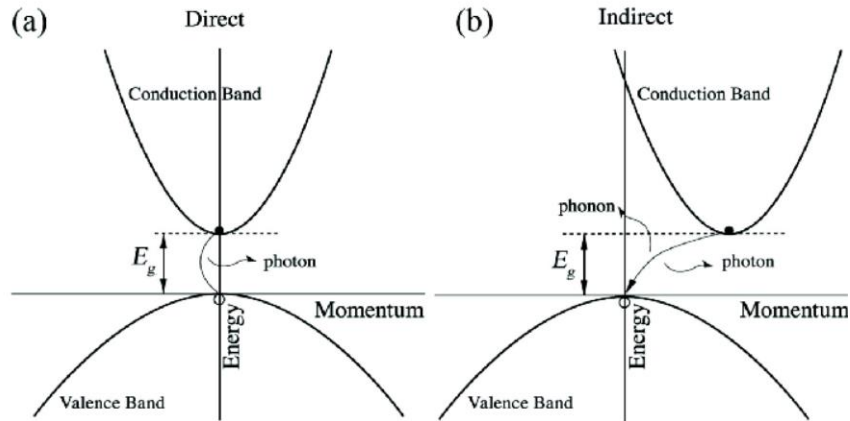


Fig. 2.3 The (a) direct and (b) indirect band gap transitions.

#### 2.2.4 Band tails

The absorption coefficient provides formidable physical information. From the  $\alpha - E$  spectra, if  $\alpha$  exhibits constant trend of variation with changing the photon energy, this is called the absorption saturation. In the low energy region, if  $\alpha$  exhibits an increasing trend of variation as the photon energy decreases, this indicates the existence of free carrier absorption. While when  $\alpha$

exhibits decreasing trend of variation with decreasing the photon energy, this indicates the presence of band tails [34].

Along the absorption coefficient curve and near the optical band edge there is an exponential part dependence on the absorption coefficient spectra and photon energy called the Urbach tail (band tail) [35, 36]. Urbach rules are described as follow [37],

$$\alpha = \alpha_o e^{E/E_e} \quad (2.15)$$

Where  $\alpha$  is the absorption coefficient,  $\alpha_o$  is a constant;  $E$  is the photon energy; and  $E_e$  is the width of the band tail of the localized state associated with the amorphous state. Taking the logarithm of the two sides of the equation (2.15), we can obtain a straight line equation. It is given by:

$$\ln(\alpha) = \ln(\alpha_o) + \frac{E}{E_e} \quad (2.16)$$

The  $E_e$  can be obtained by taking the reciprocal of the linear slope of  $\ln(\alpha) - E$  variations.

### 2.2.5 Dielectric constant spectra

The complex dielectric function and complex optical conductivity are introduced through Maxwell's equations (assuming no charge density in the absence of incident light) [38].

$$\vec{\nabla} \times \vec{E} = -\frac{\partial \vec{B}}{\partial t} \quad (2.17)$$

$$\vec{\nabla} \times \vec{H} = \vec{j} + \frac{\partial \vec{D}}{\partial t} \quad (2.18)$$

$$\vec{\nabla} \cdot \vec{B} = 0 \quad (2.19)$$

$$\vec{\nabla} \cdot \vec{D} = 0 \quad (2.20)$$

Where  $\vec{E}$ ,  $\vec{H}$ , and  $\vec{J}$  are the electric field, magnetic field, and current density, respectively. While  $\vec{D}$  and  $\vec{B}$  are the electric and magnetic fields in the medium. In linear optics, the equations relating  $\vec{D}$ ,  $\vec{B}$ , and  $\vec{J}$  to the  $\vec{H}$  and  $\vec{E}$  fields can be written in the form

$$\vec{D} = \epsilon \vec{E} \quad (2.21)$$

$$\vec{B} = \mu \vec{H} \quad (2.22)$$

$$\vec{J} = \sigma \vec{E} \quad (2.23)$$

Equations (2.21), (2.22) and (2.23), respectively, are defined the concepts of the complex dielectric function ( $\epsilon$ ), the complex magnetic permeability ( $\mu$ ), and the complex electrical conductivity ( $\sigma$ ).

Take the curl of equation (2.17) and eliminate  $\vec{B}$  and  $\vec{\nabla} \times \vec{H}$  from equations (2.22) and (2.18), respectively. This gives us

$$\vec{\nabla} \times (\vec{\nabla} \times \vec{E}) = -\mu \left( \frac{\partial \vec{J}}{\partial t} + \frac{\partial^2 \vec{D}}{\partial t^2} \right) \quad (2.24)$$

Equations (2.23) and (2.21) are substituted into equation (2.24) to obtain

$$\vec{\nabla} \times (\vec{\nabla} \times \vec{E}) = -\left( \mu \sigma \frac{\partial \vec{E}}{\partial t} + \mu \epsilon \frac{\partial^2 \vec{E}}{\partial t^2} \right) \quad (2.25)$$

This vector identity can be used to simplify the left side of equation (2.25)

$$\vec{\nabla} \times (\vec{\nabla} \times \vec{E}) = \vec{\nabla}(\vec{\nabla} \cdot \vec{E}) - \vec{\nabla}^2 \vec{E} \quad (2.26)$$

When there is no charge density,  $\vec{\nabla} \cdot \vec{E}$  equals zero, then the equation (2.26) becomes

$$\vec{\nabla}^2 \vec{E} = \mu\sigma \frac{\partial \vec{E}}{\partial t} + \mu\varepsilon \frac{\partial^2 \vec{E}}{\partial t^2} \quad (2.27)$$

By taking the curl of equation (2.18) and removing  $\vec{\nabla} \times \vec{J}$  and  $\vec{\nabla} \times \vec{D}$  from equations (2.23) and (2.21), respectively, yields

$$\vec{\nabla}^2 \vec{H} = \mu\sigma \frac{\partial \vec{H}}{\partial t} + \mu\varepsilon \frac{\partial^2 \vec{H}}{\partial t^2} \quad (2.28)$$

Equations (2.27) and (2.28) have sinusoidal solutions in the form of

$$\vec{E} = E_0 e^{i(\vec{k} \cdot \vec{r} - \omega t)} \quad (2.29)$$

$$\vec{H} = H_0 e^{i(\vec{k} \cdot \vec{r} - \omega t)} \quad (2.30)$$

Where  $\vec{K}$  is the complex propagation constant and  $\omega$  is the light's frequency. The complex propagation constant has an imaginary element that corresponds to energy dissipation and represents the attenuation of the wave inside the material, while the real part can be expressed as a wave vector.

Substituting equation (2.29) into equation (2.27) to get

$$K^2 = \mu\varepsilon\omega^2 + i\mu\varepsilon\sigma \quad (2.31)$$

When there are no energy losses,  $K$  would be a real number that may be recognized as a wave vector as

$$K_0 = \omega\sqrt{\mu\varepsilon} \quad (2.32)$$

When there is energy losses in the conducting medium,  $K$  would be a complex number defined as

$$K = w\sqrt{\mu\epsilon_{complex}} \quad (2.33)$$

Given that the complex dielectric function is defined as

$$\epsilon_{complex} = \epsilon + \frac{i\sigma}{w} = \epsilon_r + i\epsilon_{im} \quad (2.34)$$

Where  $\epsilon_r$  and  $\epsilon_{im}$  are the real and imaginary parts of the dielectric constant.

$$\epsilon_{complex} = \frac{i}{w} \left[ \sigma + \frac{\epsilon w}{i} \right] = \frac{i}{w} \sigma_{complex} \quad (2.35)$$

Here, complex conductivity was defined as

$$\sigma_{complex} = \sigma - iw\epsilon \quad (2.36)$$

Both the complex dielectric function and the complex conductivity are connected to laboratory-measured observables like absorption as well as solid-material characteristics like effective mass and carrier density. In order to get these relations, let us consider a wave that is propagating in the direction of  $z$ -axis. Equation (2.29) can be solved by substituting  $K$  to obtain a plane wave in the following form

$$\vec{E}(z, t) = E_0 e^{-iwt} e^{i w z \sqrt{\epsilon \mu} \sqrt{1 + \frac{i\sigma}{\epsilon w}}} \quad (2.37)$$

In the free space,  $\epsilon = \epsilon_0, \mu = \mu_0, \sigma = 0$ . A simple plane wave solution can be obtained from equation (2.37).

$$\vec{E} = E_0 e^{i(kz - wt)} \quad (2.38)$$

Since  $K = K_0 = w\sqrt{\epsilon_0\mu_0}$

The equation (2.37) can be expressed as follows if the electromagnetic wave is traveling through a medium with finite electrical conductivity.

$$E(z, t) = E_0 e^{\frac{-w\tilde{k}z}{c}} e^{i\left(\frac{w\tilde{n}z}{c} - wt\right)} \quad (2.39)$$

Where  $c = \frac{1}{\sqrt{\mu_0 \epsilon_0}}$ , since  $c$  is the speed of electromagnetic wave in free space and  $\tilde{k}$ ,  $\tilde{n}$  are the imaginary and real parts of the complex refractive index, respectively, which is defined as

$$\tilde{N}_{complex} = c \sqrt{\mu \epsilon \left(1 + \frac{i\sigma}{w\epsilon}\right)} = \tilde{n}(w) + i\tilde{k}(w) \quad (2.40)$$

The ratio of light speed in free space to light speed in the medium is known as the real part of refractive index ( $\tilde{n}$ ) [38]. Since the imaginary part ( $\tilde{k}$ ) indicates the amount of light absorbed at a specific wavelength, it is also known as the extinction coefficient [38]. Both the real and imaginary parts are frequency-dependent. The relation between the refractive index and the optical wavelength is introduced by an equation called the dispersion equation. The dispersive refractive index can be written as [39],

$$\begin{aligned} \tilde{N}_{complex} &= \tilde{n}(w) + i\tilde{k}(w) \\ &= (\epsilon_r + i\epsilon_{im})^{1/2} \end{aligned} \quad (2.41)$$

Where  $\epsilon_r$  and  $\epsilon_{im}$  is the real and imaginary dielectric constants, respectively. Equation (2.41) indicates that the dispersive refractive index involves some imaginary terms. This explains the optical attenuation and dispersion that the propagating electromagnetic waves through the dielectric solid undergo.

The effective dielectric constant  $\epsilon_{eff}$  can be expressed in terms of real  $\epsilon_r$  and imaginary  $\epsilon_{im}$  dielectric constants as follows [40],

$$\varepsilon_{eff} = \varepsilon_r + i\varepsilon_{im} \quad (2.42)$$

The effective dielectric constant  $\varepsilon_{eff}$  is expressed also in terms of the refractive index  $n(\omega)$  through the relation [40],

$$\varepsilon_{eff} = \tilde{n}^2(\omega) \quad (2.43)$$

By squaring both sides of equation (2.41), then comparing the real and imaginary parts on both sides of the equation, we can immediately get  $\varepsilon_r$  and  $\varepsilon_{im}$  in terms of  $\tilde{n}(\omega)$  and  $\tilde{k}(\omega)$ .

$$\tilde{n}^2(\omega) - \tilde{k}^2(\omega) = \varepsilon_r \quad (2.44)$$

$$2 \tilde{n}(\omega) \tilde{k}(\omega) = \varepsilon_{im} \quad (2.45)$$

Now, replacing  $\tilde{n}^2(\omega)$  by  $\varepsilon_{eff}$  in equation (2.44) and  $\tilde{n}(\omega)$  by  $\varepsilon_{eff}^{1/2}$  in equation (2.45), then we get the real and imaginary dielectric constants as follows [40],

$$\varepsilon_r = \varepsilon_{eff} - \tilde{k}^2(\omega) \quad (2.46)$$

$$\varepsilon_{im} = 2 \varepsilon_{eff}^{1/2} \tilde{k}(\omega) \quad (2.47)$$

### 2.2.6 Drude-Lorentz model

The Drude Lorentz model views the metals' valence electrons as free electrons. The free electrons accelerate in accordance with the classical equations when an external electric field is applied. According to the classical equation of motion, the drift velocity of the free electrons is expressed as [38].

$$m \frac{dv}{dt} + \frac{mv}{\tau} = eE_0 e^{-i\omega t} \quad (2.48)$$

The electrons' acceleration is represented by the first term, the medium's frictional damping or dissipative force is described by the second term, and the driving force is described by the electric field that is time-dependent and sinusoidal. The electrons will move in the following sinusoidal fashion since the applied electric field is sinusoidal,

$$v = v_0 e^{-i\omega t} \quad (2.49)$$

Equation (2.49) is substituted into equation (2.48) to obtain

$$\left(-i\omega m + \frac{m}{\tau}\right) v_0 = eE_0 \quad (2.50)$$

So that we can write

$$v_0 = \frac{e E_0}{\frac{m}{\tau} - i\omega m} \quad (2.51)$$

We also know that the drift velocity and carrier density are related to the current density so,

$$\vec{J} = ne v_0 = \sigma E_0 \quad (2.52)$$

Substituting equation (2.51) into equation (2.52) to get

$$\sigma = \frac{ne^2 \tau}{m(1 - i\omega \tau)} \quad (2.53)$$

Assume that the free carrier mechanism is the only conduction mechanism we are currently treating. In order to get the entire complex dielectric function, we will therefore take into account all additional contributions to  $\sigma$  in terms of  $\epsilon_{\text{core}}$  (core dielectric constant).

$$\epsilon_{\text{complex}} = \epsilon_{\text{core}} + \frac{i\sigma}{\omega} \quad (2.54)$$

Substituting equation (2.53) into equation (2.54) to get

$$\epsilon_{complex} = \epsilon_{core} + \frac{i}{w} \frac{ne^2\tau}{m(1-iw\tau)} \cdot \frac{(1+iw\tau)}{(1+iw\tau)} = \epsilon_r + i\epsilon_{im} \quad (2.55)$$

Then we can write the real and imaginary parts of the dielectric constant as

$$\epsilon_r = \epsilon_{core} - \frac{ne^2\tau^2}{m(1+w^2\tau^2)} \quad (2.56)$$

$$\epsilon_{im} = \frac{ne^2\tau}{wm(1+w^2\tau^2)} \quad (2.57)$$

Where,  $w = 2\pi f$  is the angular frequency of the incident light,  $\tau$  is the average scattering time and represent the inverse of the damping coefficient and  $n$  is the free electron density.

## Chapter Three

### Experimental Details

#### 3.1 Glass cleaning

The glass slides with dimensions of  $25.4 \times 76.2$  mm and thicknesses of 1.2 mm were cleaned before use in the preparation process of the films. Firstly, some of the glasses are divided equally into small pieces of 30 mm by a glass cutter. The glasses were then manually cleaned with a softening sponge, dish-washing liquid, distilled water and alcohol. Then, the cleaned glasses were inserting in a beaker filled with Ethyl-alcohol (97%) and covered with aluminum foil. To crack proteins that are expected to be stuck onto the glass. Then, they were washed with alcohol and dried. Finally, we get sure that the glasses do not have any scratches and/or cracks on their surface. After this cleaning process, they became suitable and ready to use them as cleaned substrates to execute the evaporation process of the films.

#### 3.2: Thin films preparation

In this part, the ion coater sputtering technique was applied to form each of the SAS-00, SAS-100, and SAS-200 films. The term SAS in this thesis corresponds to a  $\text{SiO}_2$  layer coated with an Au layer and recoated with another  $\text{SiO}_2$  layer. The number 00, 100, and 200 account for the thickness of the Au layers in nanometers. First, we coated  $\text{SiO}_2$  onto the cleaned glass for 300 s to get a 50 nm-thick  $\text{SiO}_2$  film, then coated Au on the  $\text{SiO}_2$  substrate for 60 and 120 s to get SA-100 and SA-200 nm, respectively. After this, we repeat the first step and coat  $\text{SiO}_2$  for 300 s, giving us SAS-00, SAS-100, and SAS-200 films.

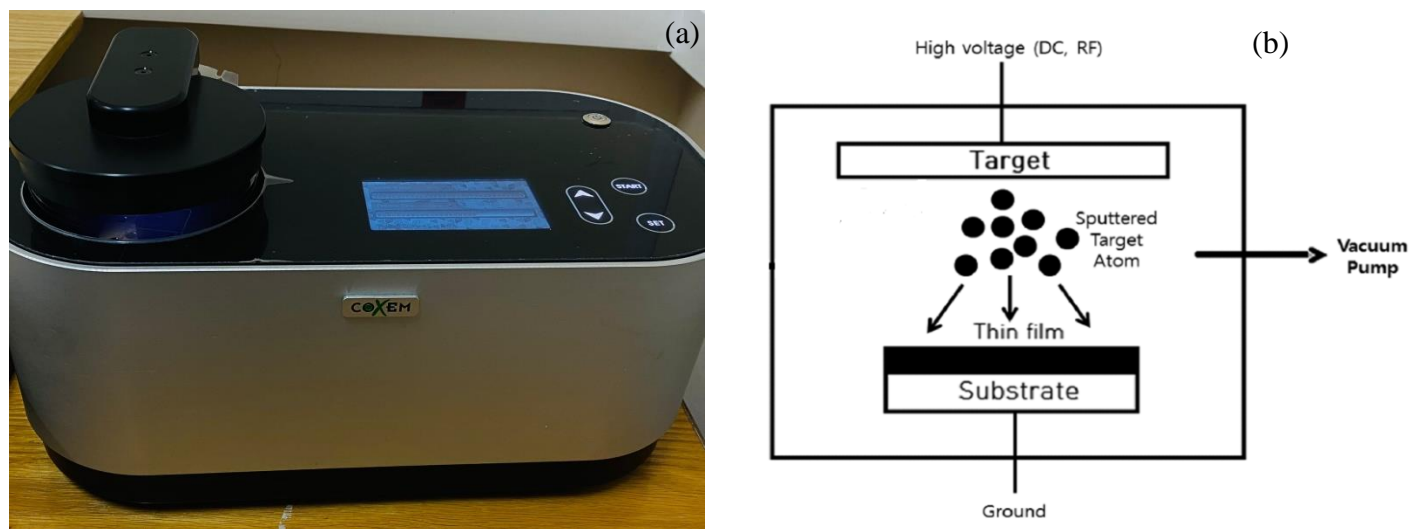


Fig. 3.1 (a) The ion coater sputtering machine (b) schematic diagram of the ion coater sputtering machine.

The thermal vapor deposition technique was applied to grow CdSe thin films onto SAS substrates under a vacuum pressure about  $10^{-5}$  mbar. Films deposited onto SAS substrates are abbreviated as SAS-00/CdSe, SAS-100/CdSe and SAS-200/CdSe. Fig. 3.2 shows the VCM 600 thermal vacuum evaporator system. First, the cleaned glass substrates, in addition to SAS-00, SAS-100, and SAS-200 substrates, were mounted close to each other on a metal plate (substrate holder). Teflon tape is used to cover about 10 mm on the edges of SAS-00, SAS-100, and SAS-200 substrates before evaporating Cadmium selenide (CdSe). Then, 0.4 gm of CdSe were weighed and then put in a boat shaped tungsten heater. After that we closed the bell jar and turned on the evaporation system. When the vacuum pressure reached  $\sim 10^{-5}$  mbar, we started the evaporation mechanism and opened the shutter after monitoring the current value and reaching 50 A. A layer of 1  $\mu\text{m}$  thick CdSe film was deposited onto the glass and SAS substrates. When the targeted thickness was achieved the shutter was closed. The thickness was monitored via an INFICON STM2 thickness–monitor attached to the system. The produced films and the remaining solid bulk that melted in the boat were maintained inside the jar until the chamber

cooled down. Then we annealed all films for 10 minutes at 250 C° in an air atmosphere to enhance their crystallinity, which initially appeared unstable and weak. The optical images and the geometrical design of the prepared films are shown in Figs. 3.3 and 3.4, respectively.



Fig. 3.2 The 600 VCM evaporation system.

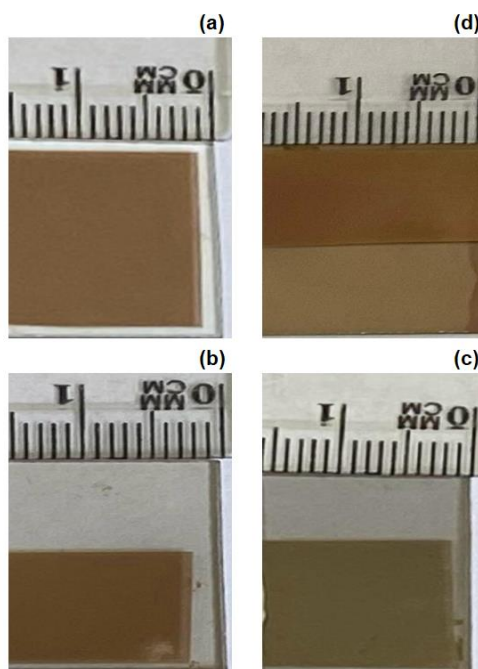


Fig. 3.3 The optical images of the real films of (a) CdSe, (b) SAS-00/CdSe, (c) SAS-100/CdSe and (d) SAS-200/CdSe films.

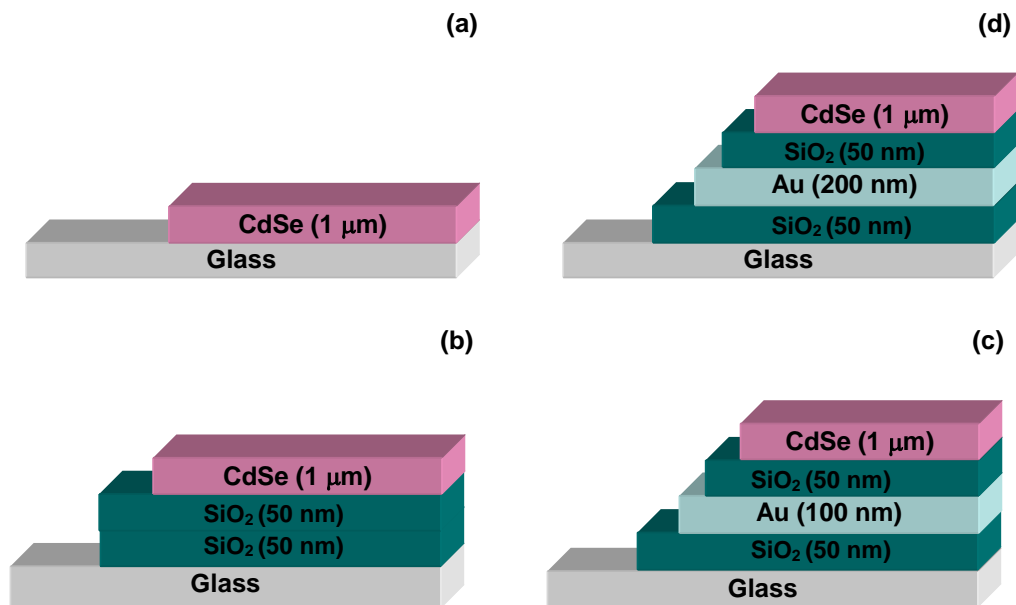


Fig. 3. 4The geometrical design of the real films of (a) CdSe, (b) SAS-00/CdSe, (c) SAS-100/CdSe and (d) SAS-200/CdSe films.

### 3.3 Thin films analysis

The prepared films were subjected to different measuring techniques in order to investigate their conductivity type, structural, optical and morphological properties. The hot probe technique, X-ray diffraction (XRD) technique, optical spectrophotometry, and scanning electron microscopy techniques were used to study these properties of the samples. These techniques are described in the following section.

### 3.3.1: The Hot Probe technique

The hot probe technique illustrated in Fig. 3.5 was used to confirm the type of conductivity (n-type or p-type) of the studied samples. This method, which consists of a heated probe and a standard digital multimeter, shows the type of semiconductor. By specifying the majority of charged carriers. The experiment is done by heating the soldering for a short period of time. A couple of cold probes and a hot probe were attached to a semiconductor surface under investigation. The hot probe is connected to the positive terminal of the multimeter and heater. As well, the cold probe was connected to the negative terminal. While the cold electrode was kept constantly connected to the surface of the sample, the hot probe was moving on its surface. When the readout voltage value in the multimeter is positive, the sample represents an n-type semiconductor. Whereas, the negative voltage value indicates that the sample under study represents a p-type semiconductor. Both CdSe and SAS-00/CdSe exhibit p-type conduction, while SAS-100/CdSe and SAS-200/CdSe exhibit n-type conduction. The conductivity type changed when evaporating CdSe on SAS-100 and SAS-200 to become n-type in both.



Fig. 3.5 The set-up of hot-probe technique.

### 3.3.2: The X-ray Diffraction (XRD) measurements

The produced CdSe, SAS-00/CdSe, SAS-100/CdSe, and SAS-200/CdSe films are structurally characterized by the Rigaku MiniFlex-600 X-ray diffraction unit. Fig. 3.6 displays the X-ray diffractometer with  $K\alpha$  radiation from a copper anode emitting XRD with an average wavelength of  $1.5405 \text{ \AA}$  at 40 KV and 15 mA. The diffraction angle  $2\theta$  was scanned between  $10^\circ$  -  $70^\circ$ , with steps of  $0.05^\circ$  and a scan speed of 1 deg/min. The data was collected using the MiniFlex support program that is connected to the X-ray diffractometer. The diffraction patterns were analyzed in accordance with Bragg's diffraction law ( $n\lambda = 2d \sin\theta$ ), where  $\lambda$  is the wavelength of the X-ray, which is  $1.5405 \text{ \AA}$ ,  $d$  is the distance between the oriented planes, and  $2\theta$  represents the positions of the diffraction peaks. The structural analysis and computer simulations are carried out by means of the "Crystdiff" and "Crystalmaker" software packages.

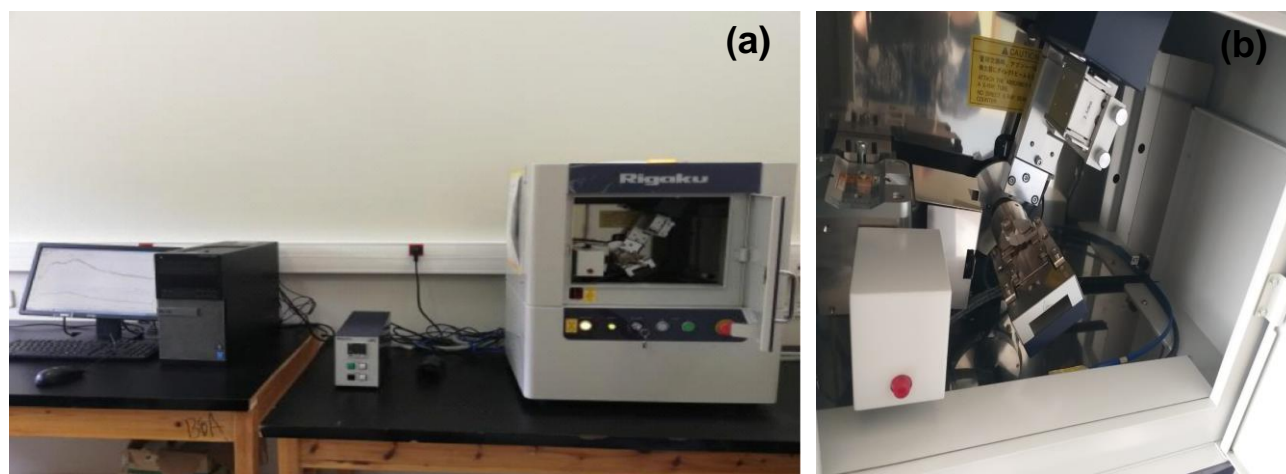


Fig. 3.6 X-ray Rigaku diffractometer.

### 3.3.3 The optical measurements

The optical transmittance and reflectance spectra of the samples were measured with the help of a Thermo Scientific Evolution 300 UV-Visible light spectrophotometer. The optical data of transmittance (T %) and reflectance (R %) spectra were measured in the range of wavelengths (300–1100 nm). The measurements were obtained at a normal incidence angle of  $15^\circ$  and a scanning speed of 1200 nm/min. The data was collected and analyzed using the Vision Pro software program, which was attached to the system as shown in Fig. 3.7. The data was applied and processed to investigate some optical parameters like the absorption coefficient ( $\alpha$ ), interband transition energies ( $E_c$ ), band tail energies, energy band gaps ( $E_g$ ), and the dielectric constant ( $\epsilon$ ).



Fig. 3.7 The UV-VIS spectrophotometer.

### 3.3.4 The morphological measurements:

Scanning Electron Microscopy (SEM) shown in Fig. 3.8 produces detailed, magnified images of an object by scanning its surface to create a high-resolution image. So, scanning electron microscopy (SEM) was used to investigate the surface morphology of CdSe, SAS-00/CdSe, SAS-100/CdSe, and SAS-200/CdSe. First, the prepared samples are coated by Pt/Au using the ion coater sputtering technique. The samples were then installed inside the microscope, and they become ready for investigation.



Fig. 3.8 The Scanning Electron Microscopy.

## Chapter Four

### Results and Discussion

#### 4.1 Structural analysis

The X-ray diffraction (XRD) patterns for standard card, CdSe, SAS-00/CdSe, SAS-100/CdSe and SAS-200/CdSe films are presented in Fig.4.1

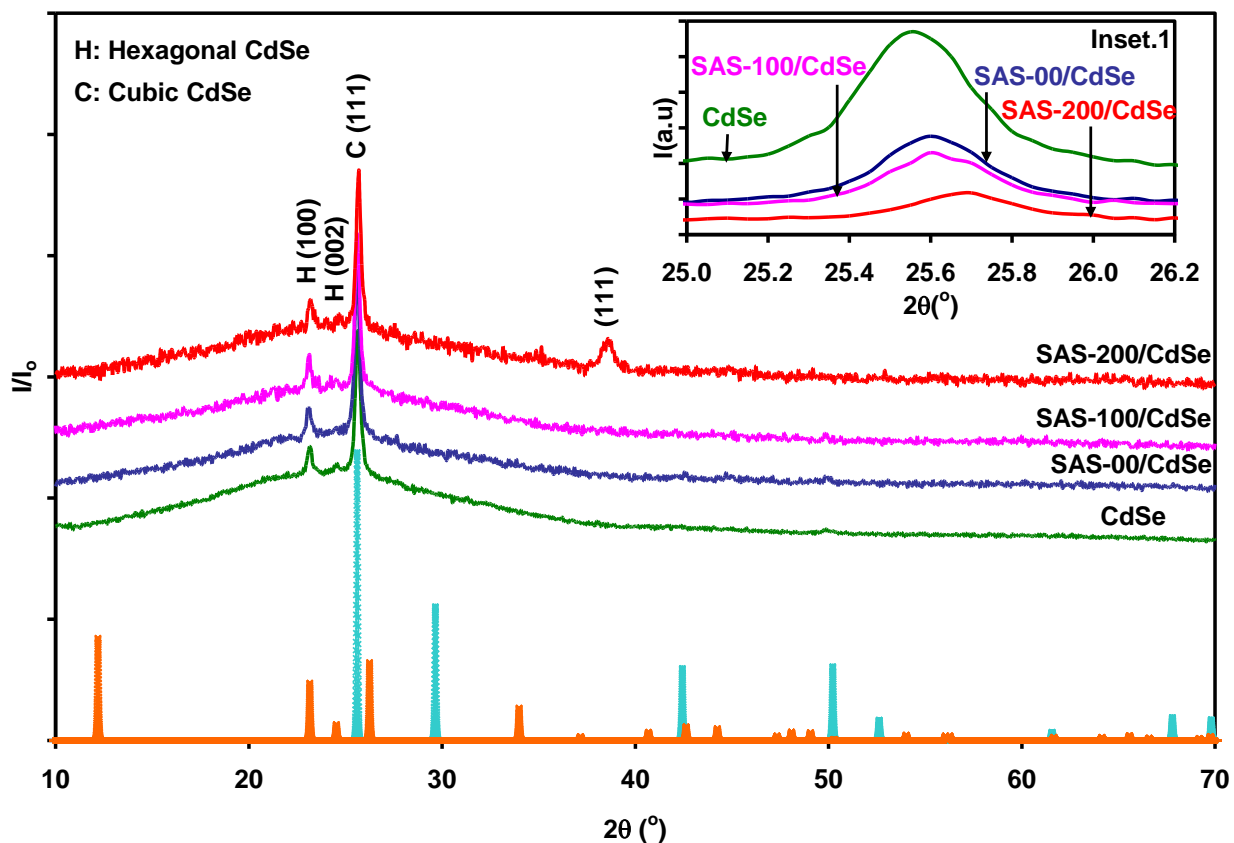


Fig. 4.1 The X-ray diffraction patterns for standard card, CdSe, SAS-00/CdSe, SAS-100/CdSe and SAS-200/CdSe films. Inset.1 shows the shift in the XRD main peak.

For CdSe film, the figure shows three peaks, with the most intensive peak observed at a diffraction angle of  $2\theta = 25.55^\circ$ . The other diffraction pattern is located at  $2\theta$  value of  $24.55^\circ$

and  $23.10^\circ$ . Analyses of the X-ray diffraction patterns in accordance with crystal diffraction software packages indicated that CdSe film has a mixed structure of hexagonal and cubic. The first and second peaks were assigned to the hexagonal structure with a space group of P3mm, shown in orange color as simulated in Figure 4.1. While the main reflection peak was assigned to the cubic structure with a space group of F-43m, which is shown in light blue color as also simulated in Figure 4.1. Since the weight percentage of hexagonal in cubic (w %) equals 35.5%.

The estimated lattice parameter in accordance with the observed reflection peaks is found to be  $a = 6.036 \text{ \AA}$ . This parameter was calculated using equation (2.2). The lattice parameters of the cubic unit cell of CdSe are comparable to those reported in the crystallography open data base as  $6.0201 \text{ \AA}$  along the a-axis of the crystalline unit cell. The analysis of the main peak indicated that the crystal planes are oriented along the C (111) direction. Other peaks which are located at diffraction angles of  $24.55^\circ$  and  $23.10^\circ$  are indexing H (100) and H (002), respectively.

The XRD patterns for SAS-00/CdSe and SAS-100/CdSe films are also shown in Fig. 4.1. Obviously, both SAS-00/CdSe and SAS-100/CdSe have the same behavior. However, we notice a decrease in the intensity of the X-ray with a very small difference in a diffraction angle. Namely it is shifted to  $25.6^\circ$ ,  $24.65^\circ$  and  $23.15^\circ$ . Such shift led to a decrease in the lattice parameter to  $a = 6.025 \text{ \AA}$ .

As Fig. 4.1 also illustrates, a number of peaks are also observed for the XRD patterns of the SAS-200/CdSe. Compared to the CdSe XRD pattern, the positions of the three peaks are shifted from  $23.10^\circ$ ,  $24.55^\circ$  and  $25.55^\circ$  to  $23.20^\circ$ ,  $24.75^\circ$  and  $25.70^\circ$ , respectively. The analysis of the reflection peaks for the mixed SAS-200/CdSe film indicated a decrease in the lattice constants

along the  $a$ -axis as a result of evaporating the CdSe layer onto SAS-200 substrate. The XRD analysis revealed a value of 6.002 Å for the lattice constant. In addition, a new peak was observed in the SAS-200/CdSe at  $2\theta$  of 38.60°. This peak was assigned to the face center cubic Au (JCPDS Card No. 04-0784) [41, 42]. Which is indexed in the (111) direction.

In order to understand the variations associated with evaporating CdSe onto glass substrate and SAS-XX/CdSe, crystallite size ( $D$ ), strain ( $\epsilon$ ), defect density ( $\delta$ ), and stacking faults (SF %) were calculated from the maximum peak broadening and diffraction position for CdSe, SAS-00/CdSe, SAS-100/CdSe and SAS-200/CdSe films are presented in Table 4.1. The structural parameters were calculated with the help of equations (2.3) – (2.6) reported in Chapter 2. As illustrated in Table 4.1, evaporating CdSe on the SAS-XX substrate causes a reduction in the values of strain, stacking faults, and defect density along both of the  $a$  and  $c$  – axis. Particularly, the substitution of some Si in vacant sites of CdSe reduces the strain, stacking faults, and defect density as we observed in Table 4.1. This substitution is owed to the fact that the ionic radius of  $\text{Se}^{-2}$  (1.98 Å<sup>o</sup>) [43] is larger than that of  $\text{Cd}^{+2}$  (0.96Å<sup>o</sup>) [44], which is larger than the ionic radius of  $\text{Si}^{+4}$ (0.56 Å<sup>o</sup>) [45], and the bond length between Cd-Se 2.62 Å<sup>o</sup> [46] is larger than Si-Se 2.28 Å<sup>o</sup> [47]. It means that Si can fill vacant sites of Cd forming stronger bonds of Si-Se rather than Cd-Se. As the thickness of the Au layer increases, there is a noticeable reduction in strain and a decrease in defect density.

Table 4.1 The structural parameters of the main peak of CdSe, SAS-00/CdSe, SAS-100/CdSe and SAS-200/CdSe.

Sample	$2\theta(^{\circ})$	$I(\times 10^3 \text{ c/s})$	Miller indices			A	D (nm)	$\epsilon \times 10^{-3}$	SF%	$\delta (\times 10^{11} \text{ line/cm}^2)$
			h	k	l					a-axis
CdSe	25.6	5.695	1	1	1	6.036	24	6.71	0.323	6.824
SAS-00/CdSe	25.6	2.768	1	1	1	6.025	24	6.68	0.322	6.797
SAS-100/CdSe	25.6	2.304	1	1	1	6.025	24	6.68	0.322	6.797
SAS-200/CdSe	25.7	1.171	1	1	1	6.002	25	6.63	0.32	6.742

Particularly, as seen in Table 4.2, as the ionic radius of  $\text{Se}^{-2}$  ( $1.98 \text{ \AA}$ ) [43] is larger than that of  $\text{Cd}^{+2}$  ( $0.96 \text{ \AA}$ ) [44], the ionic radius of  $\text{O}^{-2}$  ( $1.36 \text{ \AA}$ ) [17] is less than that of  $\text{Se}^{-2}$ , and the bond lengths (listed in Table 4.3) of Cd-Cd, Cd-Se, Cd-O, Si-Si, Si-Se, Si-O, and Se-Se are  $6.54 \text{ \AA}$  [48],  $2.62 \text{ \AA}$  [46],  $2.35 \text{ \AA}$  [45],  $2.35 \text{ \AA}$  [49],  $2.28 \text{ \AA}$  [47],  $1.62 \text{ \AA}$  [49] and  $2.29 \text{ \AA}$  [50], respectively. The bonding between the Cd and O atoms is much stronger than that between Cd and Se. These properties make the Cd atoms have the tendency to move toward oxygen atoms, forcing them to form CdO bonds. This causes clusters and grains inside the material, which lead to a decrease in defects. It is clear from the presented structural data that insertion of Au nanosheet between stacked layers of  $\text{SiO}_2$  slightly induced crystallinity of CdSe. Actually as seen from Table 4.4, the electronic configuration of Au reaches  $5d^{10}6s^1$  [32] which is at higher atomic orbitals than Si ( $3s^23p^2$ ) [51]. The orbital overlapping between Si and Au atomic orbitals enhance the electrical conductivity significantly and allows the existence of many free electrons on the surface. As a results as, substrates behave like metals leading to an induced crystallites process in CdSe.

Table 4.2 The ionic radius of Cd, Se, Si, O and Au atoms.

Sample	ionic radius( $\text{A}^\circ$ )
$\text{Cd}^{+2}$	0.96
$\text{Se}^{-2}$	1.98
$\text{Si}^{+4}$	0.56
$\text{O}^{-2}$	1.36
$\text{Au}^{+1}$	1.37

Table 4.3 The bond length and the bond energy of the bonding atoms.

Bond	Bond length ( $\text{A}^\circ$ )	Bond energy (KJ/mole)
Cd-Cd	6.54	127.10
Cd-Se	2.62	127.60
Cd-O	2.35	236.38
Si-Si	2.35	226.00
Si-Se	2.28	427.86
Si-O	1.62	460.00
Se-Se	2.29	172.00

Table 4.4 The electronic configuration of Cd, Se, Si, O and Au atoms.

Sample	electronic configuration
Cd	$[\text{Kr}] 4d^{10}5s^2$
Se	$[\text{Ar}] 3d^{10}4s^24p^4$
Si	$[\text{Ne}] 3s^2 3p^2$
O	$[\text{He}] 2s^22p^4$
Au	$[\text{Xe}]4f^{14}5d^{10}6s^1$

## 4.2 Morphological analysis

Scanning electron microscopy (SEM) is a helpful instrument for studying thin-film microstructures. Also, the range of the grain sizes and the surface shape were examined using SEM. The surface morphology of CdSe, SAS-00\CdSe, SAS-100\CdSe, and SAS-200\CdSe was illustrated in Fig.4.2 and Fig.4.3. The SEM image of the SAS-00/CdSe sample being enlarged by 54 and recorded at 25 KV is shown in Fig. 4.2 (a). The general form of SAS-00/CdSe film is indicated in Fig. 4.2 (a). Additionally, Fig. 4.2 (a) makes clear the presence of a few clusters that vary in size and shape. These clusters have been enlarged in Fig. 4.2 (b, c, and d). Fig. 4.2 (b) represents the surface morphology of SAS-00/CdSe film on enlarge for 1K times and recorded at 25 KV. It is clear from Fig. 4.2 (b) that there is a process of nanowire formation. Fig. 4.2 (c) displays an elliptical cluster of grains with varying sizes and shapes, such as spherical, flower-like, and other random shapes. Fig. 4.2 (d) exhibits the SEM image of SAS-00/CdSe film on enlarge for 2.3K time. Which represents a region composed of  $3.4 \text{ nm}^2$  of flower-like grains.

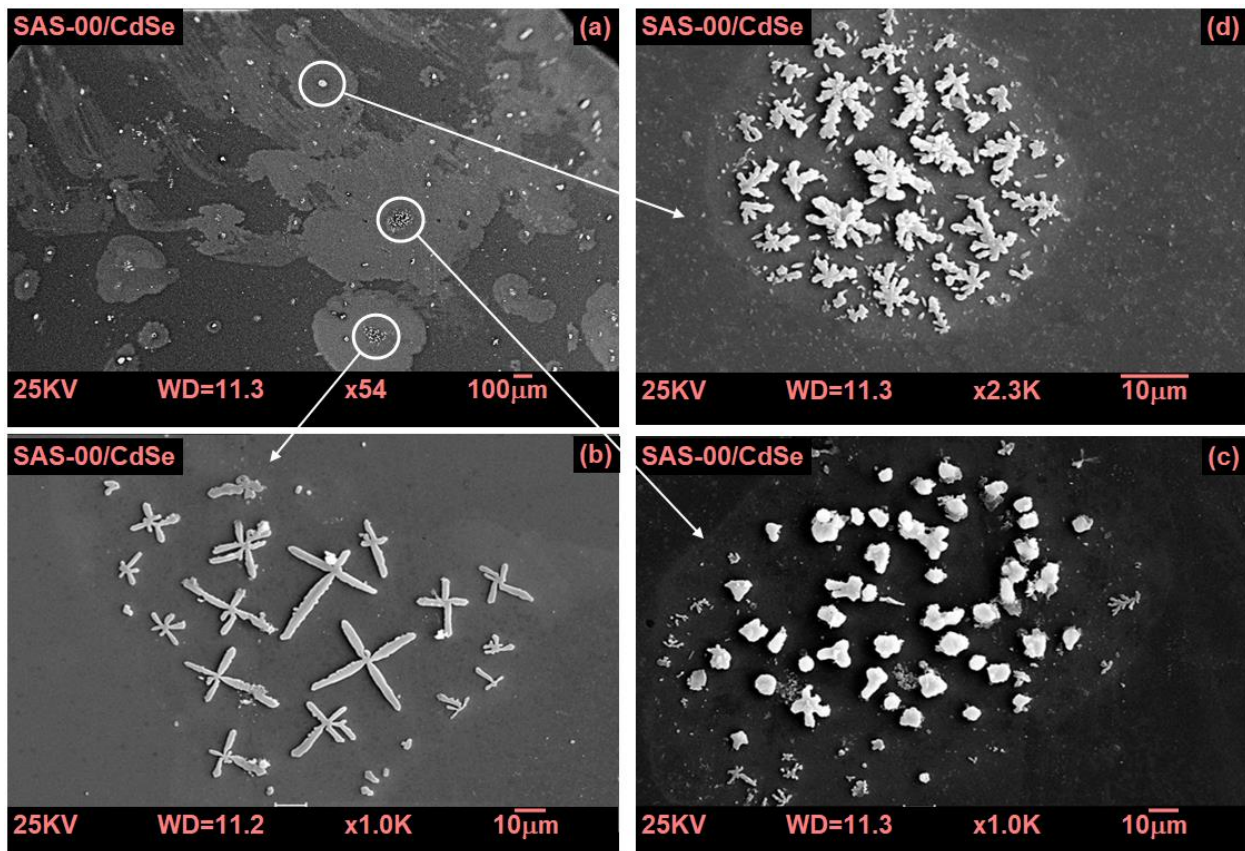


Fig. 4.2 SEM image for sample (a) SAS-00/CdSe for 54 enlargements, (b, c) SAS-00/CdSe for 1K enlargement in different sites, and (d) SAS-00/CdSe for 2.3K enlargement

Moreover, Fig. 4.3 demonstrates the surface morphology of CdSe, SAS-00\CdSe, SAS-100\CdSe, and SAS-200\CdSe films. Which is enlarged by 10K and recorded at 25 KV. Fig. 4.3 (a) represents the surface morphology of CdSe film. Pure CdSe films show the distribution of very tiny and barely visible grains. Also, within the grains, circular clusters containing one or two large grains (with a diameter of 0.25  $\mu\text{m}$ ) or a few small grains (with a diameter of 0.125  $\mu\text{m}$ ) can be visible. The SEM image of the SAS-00/CdSe film is indicated in Fig. 4.3 (b). Obviously, it's different from CdSe films, and the grains become invisible. Also, a region of clusters was formed in an irregular shape, and it's almost impeded inside an amorphous sea. The

surface morphology of the SAS-100/CdSe film is shown in Fig. 4.3(c). It is evident that the addition of an Au layer with a thickness of 100 nm makes the changes more visible and causes CdSe to evolve into a nanowire form. The wires are randomly distributed with irregular lengths, with an average length of about 2.5  $\mu\text{m}$ , but mostly have the same diameter about 0.13  $\mu\text{m}$ . Fig. 4.3(d) illustrated the surface morphology of SAS-200/CdSe film. Increasing the gold content inside the substrate resulted in the formation of spherical grains filling a large region exceeding 196.7  $\mu\text{m}^2$ . Below each circle, the impeded wire is still visible, but this has turned the wire length shorter, about 1  $\mu\text{m}$  and thicker with an average thickness of 0.2  $\mu\text{m}$ .

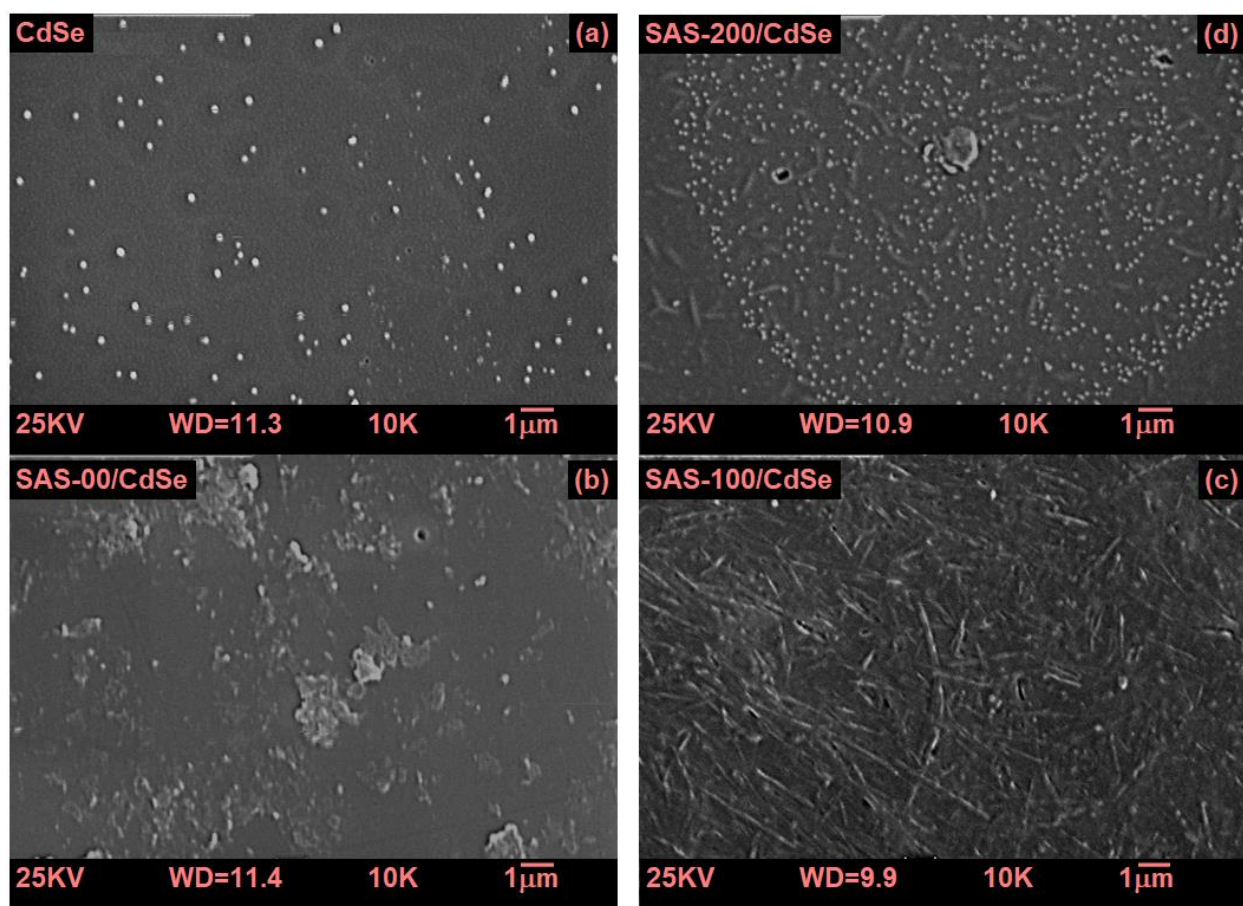


Fig. 4.3 SEM image for sample (a) CdSe, (b) SAS-00/CdSe, (c) SAS-100/CdSe, and (d) SAS-200/CdSe for 10K enlargement and recorded at 25 KV.

### 4.3 Optical analysis

The study of the optical properties of CdSe and SAS-XX/CdSe films at different thicknesses of Au 00, 100, and 200 nm is based on the thickness because the thickness of the films plays a role in the optical properties. Ultraviolet-visible light-IR spectrophotometry was used to measure the transmittance (T) and reflectance (R) spectra in the spectral wavelength ( $\lambda$ ) range of 300–1100 nm at a scanning speed of 1200 nm/min. As shown in Fig. 4.4, the transmittance spectra of the CdSe film increase with decreasing incident photon energy. The increase in the transmittance spectra reaches maximum transmittance of ~60%, and it seems to be saturated at ~60% in the low energy region. It is also shown that the SAS-00/CdSe film has the same behavior as the CdSe film. On the other hand, for SAS-100/CdSe, the transmittance spectra also increase with decreasing energy and reaches about 47% in the low energy level, but they are not saturated and slowly varying. T% for SAS-200/CdSe is also decreasing and not saturated, and the transmittance is decreasing to low transparency (~14%). We noticed that with increasing thickness, the transmittance decreased. This is considered systematic behavior due to the fact that thicker films include more atoms, which means there are more states available for photon absorption [52]. Fig. 4.4 also shows a red shift to the high wavelength area in all transmittance spectra due to interaction between degenerate (metal-like) SAS substrates and CdSe thin films.

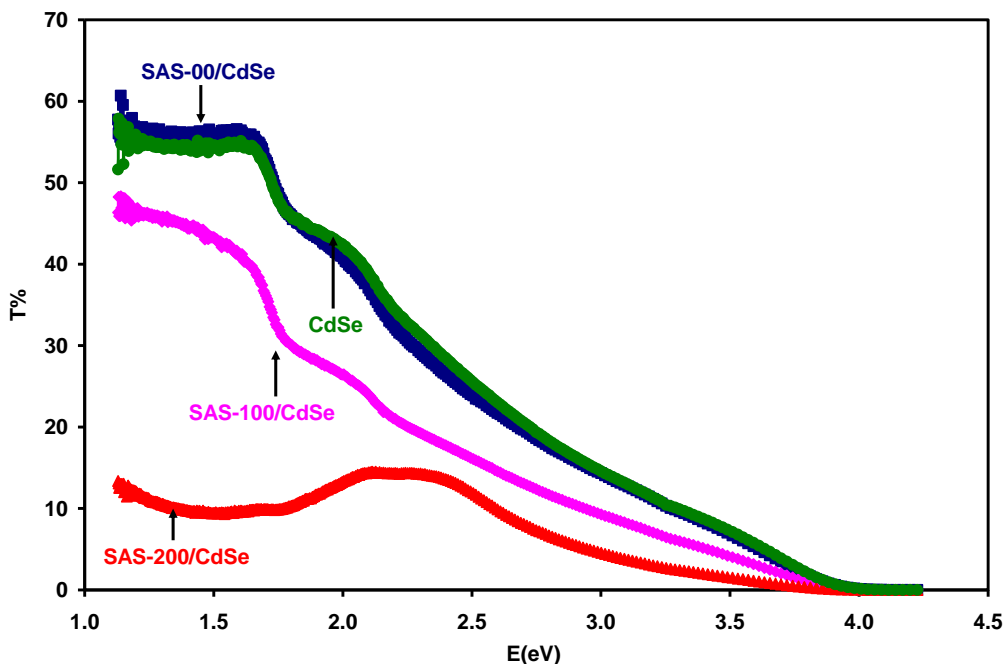


Fig. 4.4 The transmittance of CdSe, SAS-00/CdSe, SAS-100/CdSe, and SAS-200/CdSe films.

On the other hand, the reflectance spectra are presented in Fig. 4.5. Which shows that the evaporation of CdSe onto thin-layer substrates (SAS-00 and SAS-100) is less effective on the values of reflectance. But it shows different behavior as the thickness of Au increases to 200 nm. Clearly, the reflectance is highly increased to ~40%, and we also noticed that there are two peaks of maximum reflectance at 1.62 eV and 1.36 eV. There are several options that may have these variations which are related to the band gaps of CdO, CdSe, and SiO<sub>2</sub>. As we mentioned previously in Tables 4.1 and 4.2, the ionic radius of Se<sup>-2</sup> is less than that of Cd<sup>+2</sup>, the ionic radius of O<sup>-2</sup> is less than that of Se<sup>-2</sup>, and the bond lengths of Cd-Se and Cd-O are 2.62 Å and 2.35 Å, respectively. This means that O prefers to form CdO bonds, so the first choice is CdO, which has an indirect band gap of 1.36 eV [53]. CdSe may have a band gap of 1.62 eV instead of 1.74 eV due to a decrease in the value of the lattice parameter along the c-axis [54].

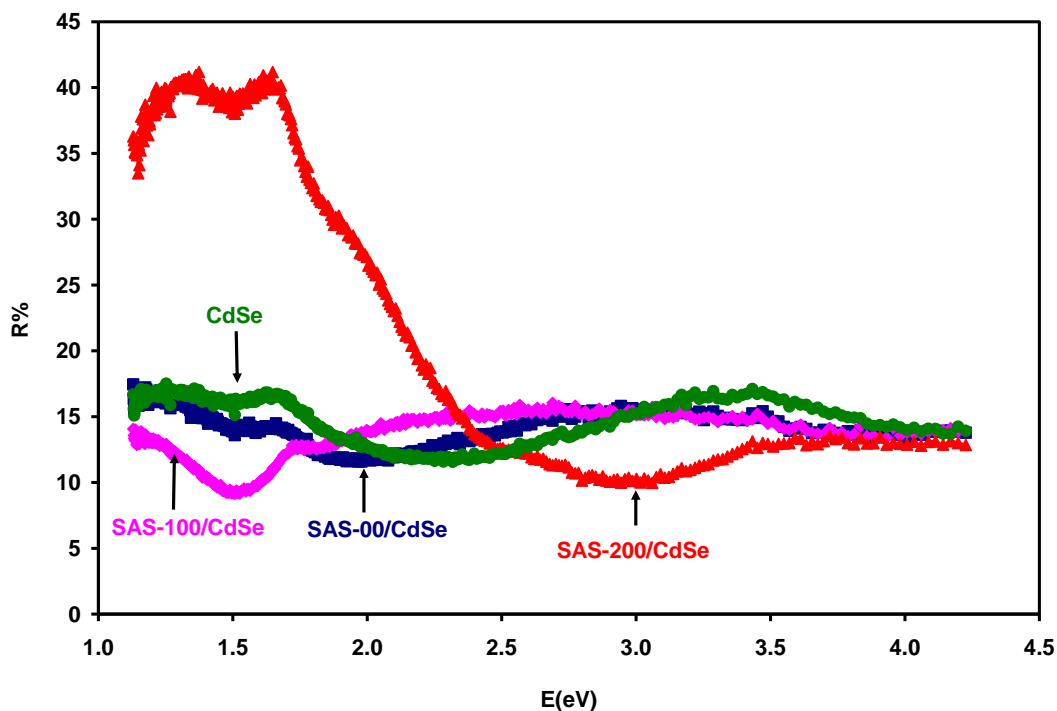


Fig. 4.5 The reflectance of CdSe, SAS-00/CdSe, SAS-100/CdSe, and SAS-200/CdSe films.

In order to get a better understanding of the optical properties of CdSe, SAS-00/CdSe, SAS-100/CdSe, and SAS-200/CdSe films, the absorption coefficients ( $\alpha$ ) spectra, were calculated from the measured transmittance (T) and reflectance (R) spectra, determined by the equations (2.13). The data are represented in Fig. 4.6. As the figure displays, the absorption coefficient spectra of all films exhibit three regions of absorption. These regions are the high absorption region in the high energy range between 4.2 – 3.6 eV. In this region, the absorption coefficient increases rapidly with increasing energy, so based on this region, we will calculate the energy band gap later. The moderate absorption region is between 3.6 – 2.0 eV and the third region is the weak absorption region in the incident photon energy range below 2.00 eV. Inset.1 shows the behavior of the absorption coefficient ( $\alpha$ ) spectra in the low-energy region. It seems that the

absorption coefficients ( $\alpha$ ) decrease with decreasing incident photon energy. A pronounced decrease in absorption coefficients ( $\alpha$ ) spectra with decreasing energy is observed for SAS-100/CdSe and SAS-200/CdSe. The slope of the  $\alpha$ - $E$  variation for these two samples is sharper at 1.15-2.00 eV than in CdSe and SAS-00/CdSe films. As seen from the figure, the spectra for the CdSe evaporated onto the SAS-200 substrates show a sharp decrease in the absorption coefficient values with decreasing photon energy starting at 1.48 eV. This behavior is attributed to the presence of some extended band tails in the energy band gap of the SAS-100/CdSe and SAS-200/CdSe films.

In that context, the presence of a large number of defects [55], vacancies, impurities, and broken bonds [56] may result in these tails. The band tails are calculated in the low absorption region with the help of Urbach rules [54] for the exponential band tail distribution, which is presented by equation (2.16). The band tail width is estimated using this formula. Taking the reciprocal of the slope value of the linear variations of  $\ln(\alpha)$  versus  $E$ , as demonstrated in Fig 4.7, reveals a band width of 0.63 eV and 0.15 eV for SAS-100/CdSe and SAS-200/CdSe, respectively. In addition to the above mentioned reasons the formation of these band tails can also be assigned to the orbital overlapping. Since the electronic configuration of Cd, Se, Si, O and Au atoms are [Kr] 4d<sup>10</sup>5s<sup>2</sup> [55], [Ar] 3d<sup>10</sup>4s<sup>2</sup>4p<sup>4</sup> [57], [Ne] 3s<sup>2</sup> 3p<sup>2</sup> [53], [He] 2s<sup>2</sup>2p<sup>4</sup> [55] and [Xe] 4f<sup>14</sup>5d<sup>10</sup>6s<sup>1</sup> [58], respectively, as shown in (Table 4.4). Then Cd atomic orbitals overlapping with these of Si in the substrate may lead to this phenomena.

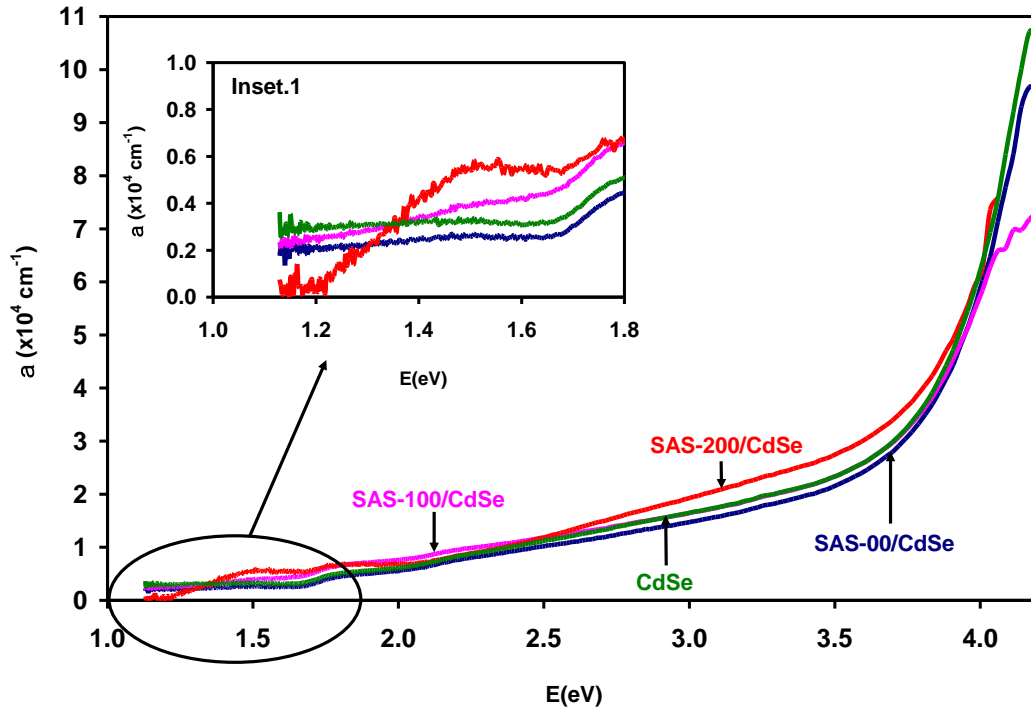


Fig. 4.6 The absorption coefficient spectra of CdSe, SAS-00/CdSe, SAS-100/CdSe, and SAS-200/CdSe films.

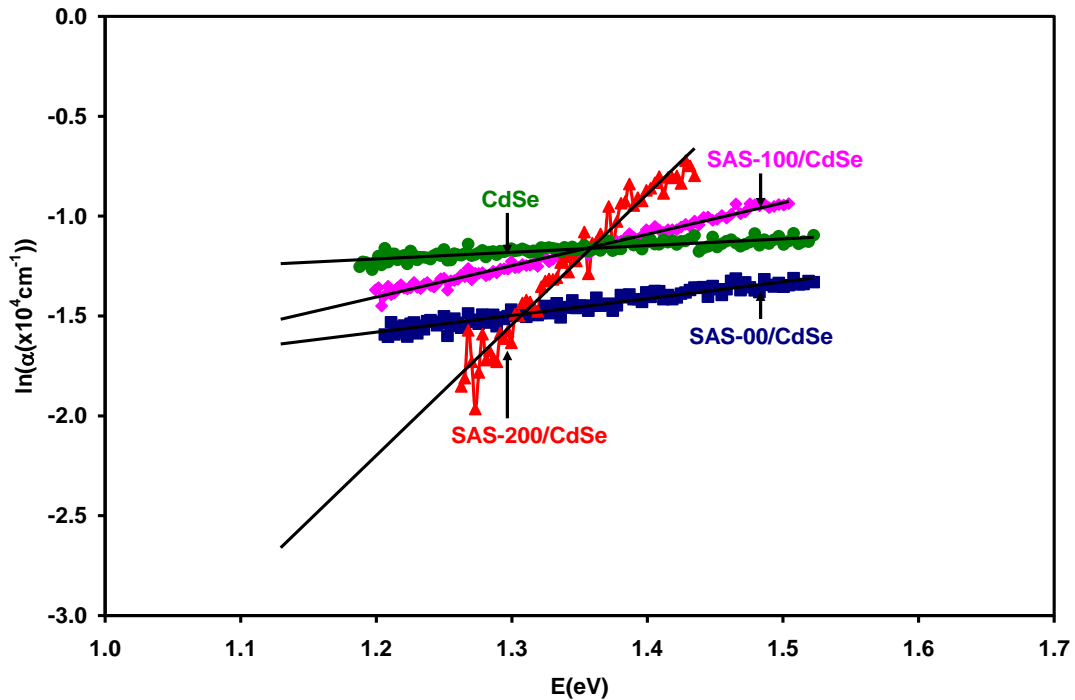


Fig. 4.7 The  $\ln(\alpha)$ -E variation in the low absorption region for band tail investigation of CdSe, SAS-00/CdSe, SAS-100/CdSe, and SAS-200/CdSe films.

The absorption coefficient spectra give information about the energy band gaps ( $E_g$ ) of CdSe and SAS-00, 100 and 200/CdSe. The effect of evaporating of CdSe on SAS-00, 100, and 200 on the optical energy band gap of CdSe film is determined with the help of Tauc's equation (2.14). The direct forbidden energy band gap for CdSe, SAS-00/CdSe, SAS-100/CdSe, and SAS-200/CdSe films interfaces was determined from the plotting of the  $\alpha E^{2/3} - E$  variations in strong absorption energy range which is presented in Fig. 4.8. In the strong absorption region, the straight solid lines which crosses the energy (E) - axis revealed energy band gap value of 1.685 eV, 1.765 eV, 1.680 eV, and 1.715 eV for CdSe, SAS-00/CdSe, SAS-100/CdSe and SAS-200/CdSe respectively. Evaporation CdSe on SAS-00 substrates increased the energy band gap from 1.685 to 1.765 eV and when increasing the thickness of Au to 100 and 200 nm, we noticed that there is no significant effect onto the optical band gap of CdSe in this region. Assuming a percentage error of 5% in the calculation then it is possible to think that the substrates play no role on  $E_g$  value.

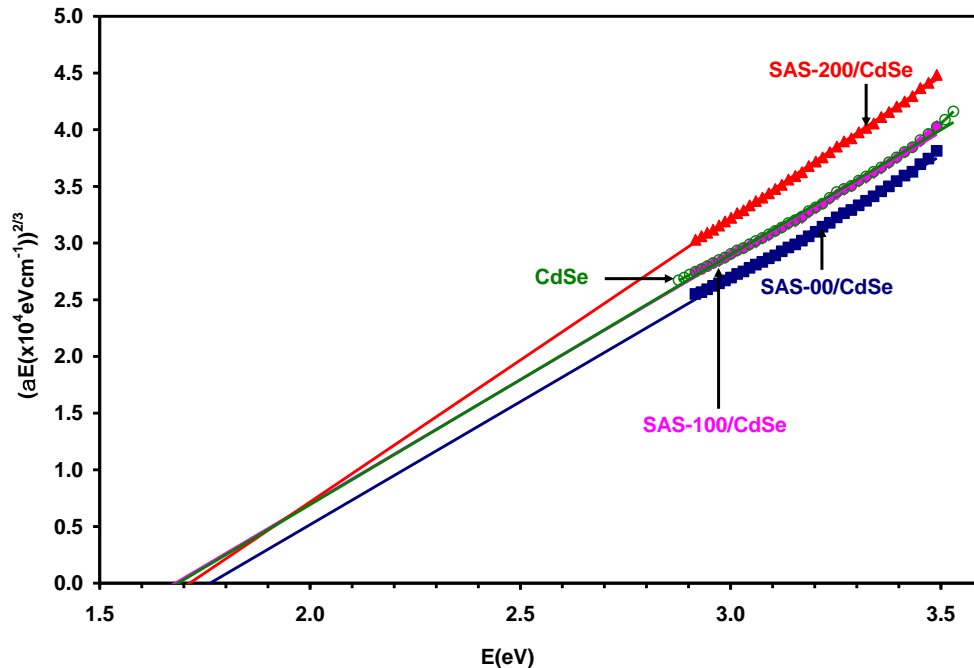


Fig. 4.8 The  $(\alpha E)^{2/3} - E$  in the strong absorption region for CdSe, SAS-00/CdSe, SAS-100/CdSe and SAS-200/CdSe

But if we returning back to the weak absorption region and assuming that a new band gap was formed then, Fig. 4.9 reveals a band gap value of 1.13 eV in SAS-200/CdSe film. This energy band gap is regarded as being for Si. [59]

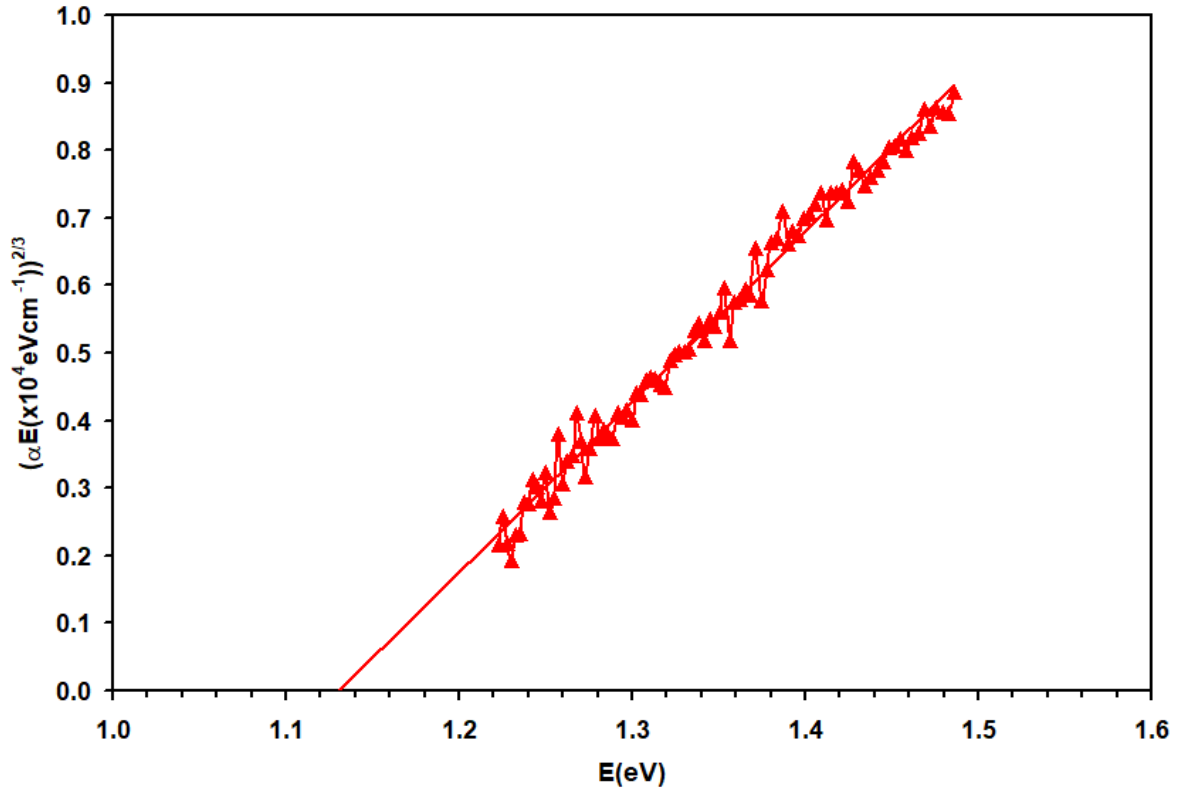


Fig. 4.9 The  $(\alpha E)^{2/3} - E$  in the weak absorption region for SAS-200/CdSe.

The absorption coefficient ratio (absorbability) was calculated with the equation  $R_\lambda \% = \left( \frac{\alpha_{SAS-XX/CdSe}}{\alpha_{CdSe}} \right)$  and presented in Fig. 4.10. The figure shows an interesting result. As

illustrated in Fig. 4.10, the light absorbability of SAS-00/CdSe increased in all ranges, but it reached ~38% in the infrared range. As also illustrated in Fig. 4.10, the light absorbability of SAS-100/CdSe was enhanced in the infrared range and reached ~ 41% at 1.66 eV, then back to

decrease in each of the infrared, visible, and UV ranges. It's noticeable that for SAS-200/CdSe, the light absorbability is enhanced in all ranges; in the visible range, it becomes ~20%. It also becomes ~86% and reaches ~100% in the infrared range. These enhancements are based on various reasons, including reduced defect concentration, increased free charge carrier concentration, orbital overlapping, and surface plasmon resonance [60].

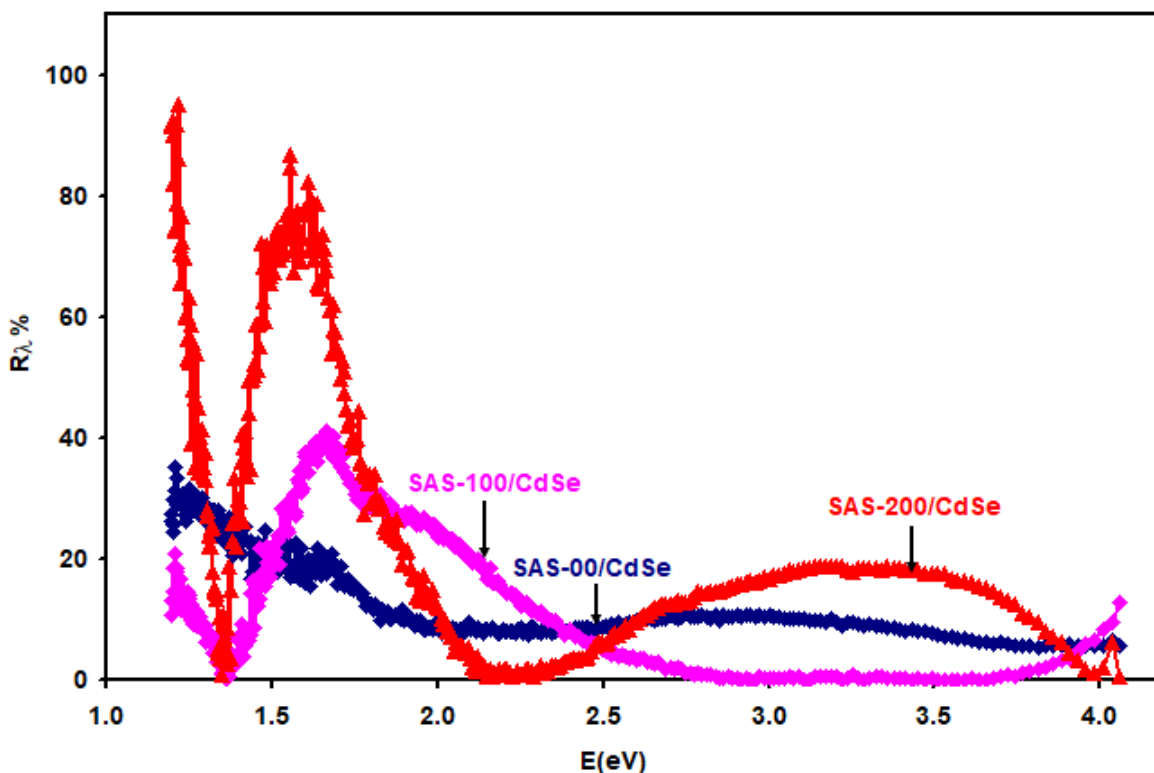


Fig. 4.10 The light absorbability for SAS-00/CdSe, SAS-100/CdSe and SAS-200/CdSe.

#### 4.4 Dielectric analysis

To investigate possible applications of the SAS-XX/CdSe, the respective real ( $\epsilon_r$ ) and imaginary ( $\epsilon_{im}$ ) parts of the relative dielectric spectra for the studied samples are estimated.  $\epsilon_r$  and  $\epsilon_{im}$

which are calculated using the previously described methods (equations (2.46) and (2.47)) are illustrated in Fig. 4.11 and 4.12 respectively.

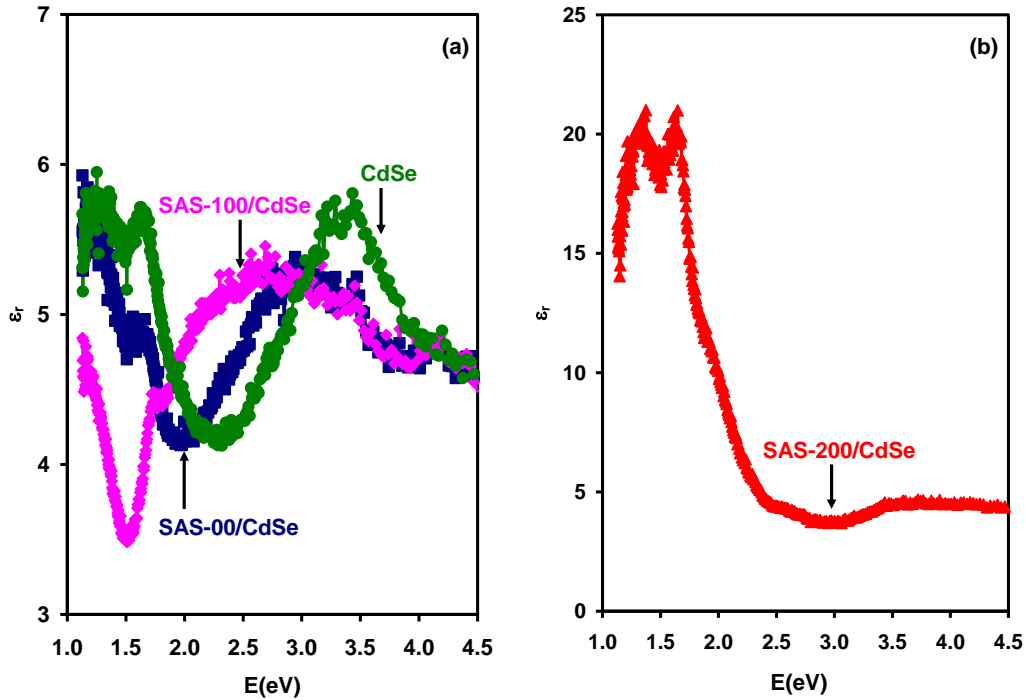


Fig. 4.11 The real part of the dielectric spectra for (a) SAS-00/CdSe, SAS-100/CdSe and CdSe films (b) SAS-200/CdSe.

As it is readable from Fig. 4.11 (a), the real part of the dielectric spectra of CdSe displays three peaks, the first one is centered at a critical energy at 3.43 eV, the second “broaden peak” is observed at 3.21 eV, and the last peak appearance at 1.62 eV. The third peak (1.62 eV) also appeared on both SAS-00/CdSe and SAS-100/CdSe, with a blue shift in this peak to 1.66 eV and 1.72 eV, respectively, accompanied by a decrease in the value of the real part of the dielectric constant. As also seen from Fig. 4.11 (b) that the dielectric spectra of SAS-200/CdSe exhibit two peaks centered at 1.36 eV and 1.62 eV. These peaks probably belong to CdO and CdSe, respectively [53, 54].

However, when compared to the imaginary part of the spectra, the imaginary part of the dielectric spectra, which are shown in Fig. 4.12, exhibits a different trend of variation. Namely, as the incident photon energy range decreases,  $\epsilon_{im}$  also decreases in the range of 4.5–2.0 eV for all films. In the low energy region, decreasing incident photon energy is still decreasing the value of  $\epsilon_{im}$  for each of the CdSe, SAS-00/CdSe, and SAS-100/CdSe films, but it shows different behavior for the SAS-200/CdSe film. It is clear from Fig. 4.12 that decreasing the incident photon energy values from 2.0–1.50 eV increases the value of  $\epsilon_{im}$ , but when decreasing the energy to ~ 1.0 eV, the value of  $\epsilon_{im}$  decreases with decreasing energy.

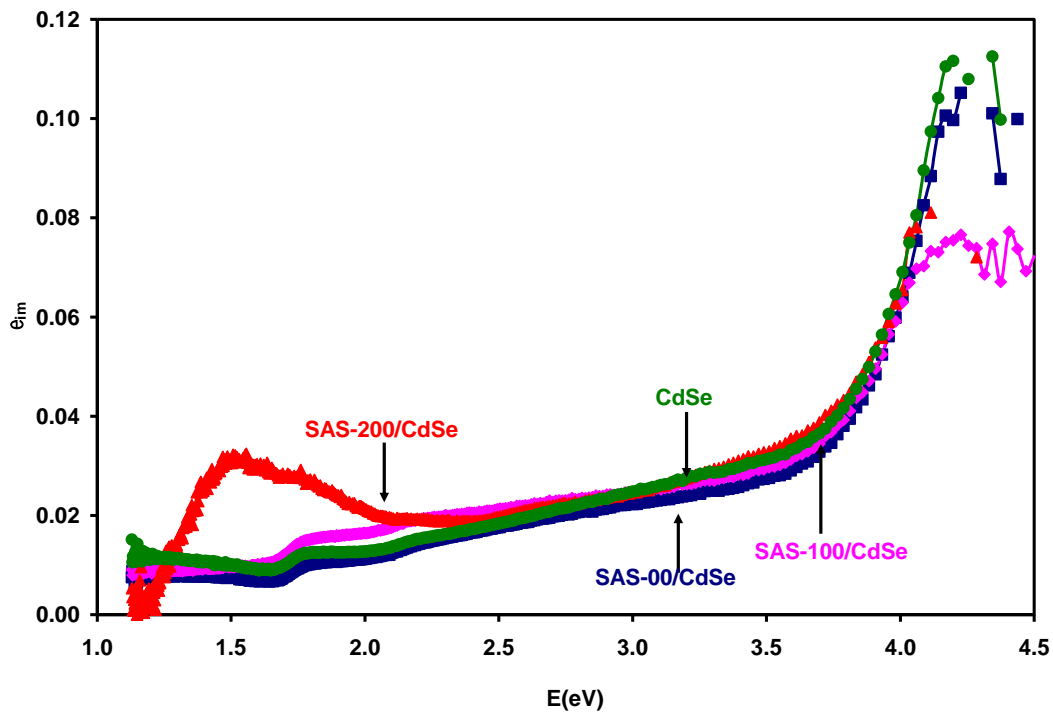


Fig. 4.12 The imaginary part of the dielectric spectra for CdSe, SAS-00/CdSe, SAS-100/CdSe and SAS-200/CdSe films.

The imaginary part of dielectric constants is important since it is directly related to optical

conductivity ( $\sigma(\omega) = \frac{\epsilon_{im}\omega}{4\pi}$ ;  $\omega$  is radial frequency and equal  $\frac{2\pi c}{\lambda}$ ) [61].

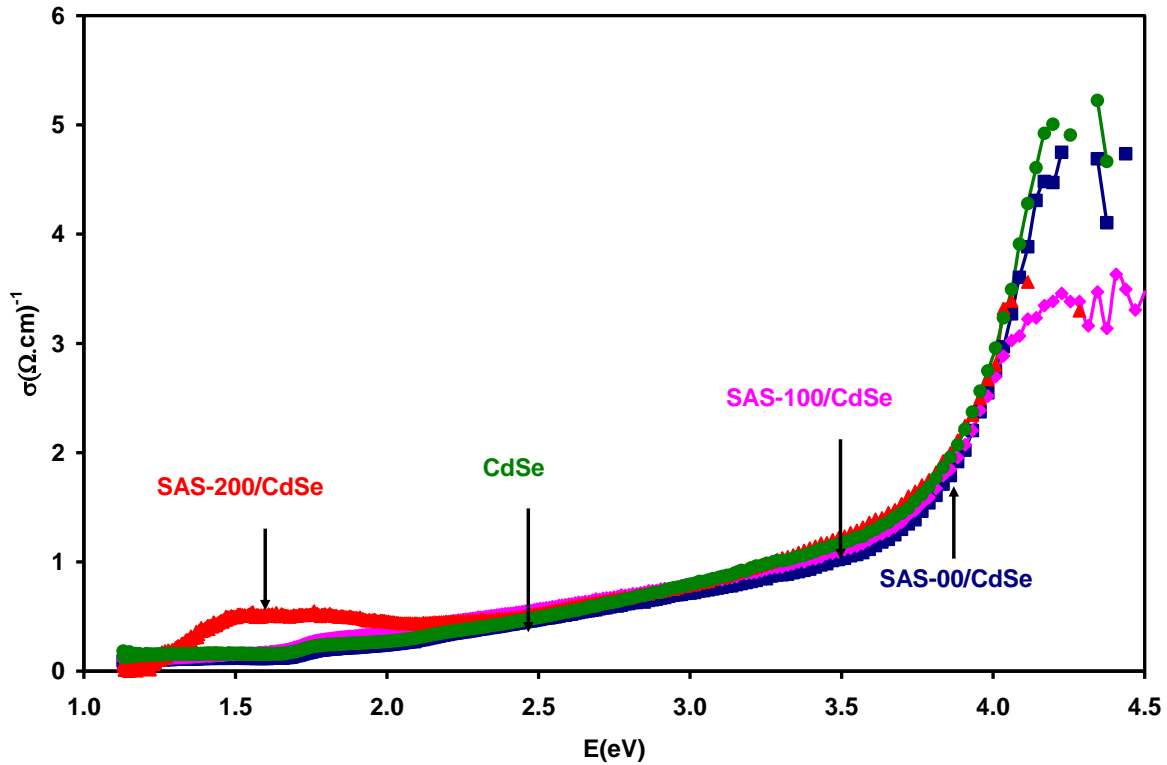


Fig. 4.13 The optical conductivity for CdSe, SAS-00/CdSe, SAS-100/CdSe and SAS-200/CdSe films.

The figure shows that an increase in photon energy corresponds to a higher  $\epsilon_{im}$  and a larger optical conductivity. It is evident from Fig. 4.13 that all films have low optical conductivity because of the strong bonds that bind their electrons together [62]. This property makes these films work well in a variety of optical and optoelectronic applications [63].

To get more information, the imaginary part that is given by the equation (2.47) was modeled according to the Drude-Lorentz model through the modeling relation

$$\left( \epsilon_{im} = \sum_{i=1}^k \frac{w_{pei}^2 w}{\tau_i ((w_{ei}^2 - w^2) + w^2 \tau_i^{-2})} \right)$$
. Where,  $k$  is the number of dominant linear oscillator,  $w_{pe} = \sqrt{4\pi n e^2 / m^*}$  is the electron bounded plasmon frequency,  $w = 2\pi f$  is the angular frequency of

the incident light,  $\tau$  is the average scattering time and represent the inverse of the damping coefficient and  $w_e$  is the reduced resonant frequency.  $n$  is the free electron density and  $m^*$  is the free carrier effective mass. In this model, assuming the hole effective mass in the  $\text{SiO}_2$  is to be  $0.58 m_0$  [64], the hole effective mass of  $\text{CdSe}$  is  $0.45 m_0$  [65] and the effective mass of  $\text{Au}$  equals  $1.10 m_0$  [66], then the reduced mass for the  $\text{SAS-00/CdSe}$  and  $\text{SAS-100,200/CdSe}$  films is  $0.17 m_0$  and  $0.15 m_0$ , respectively. The fitting of the imaginary part equation assuming the presence of six oscillators ( $k = 6$ ) is shown by the brown line in Fig. 4.14. A good correlation between the theoretical and experimental spectral data is obtained via the fitting parameters, which are calculated and tabulated in Table 4.5.

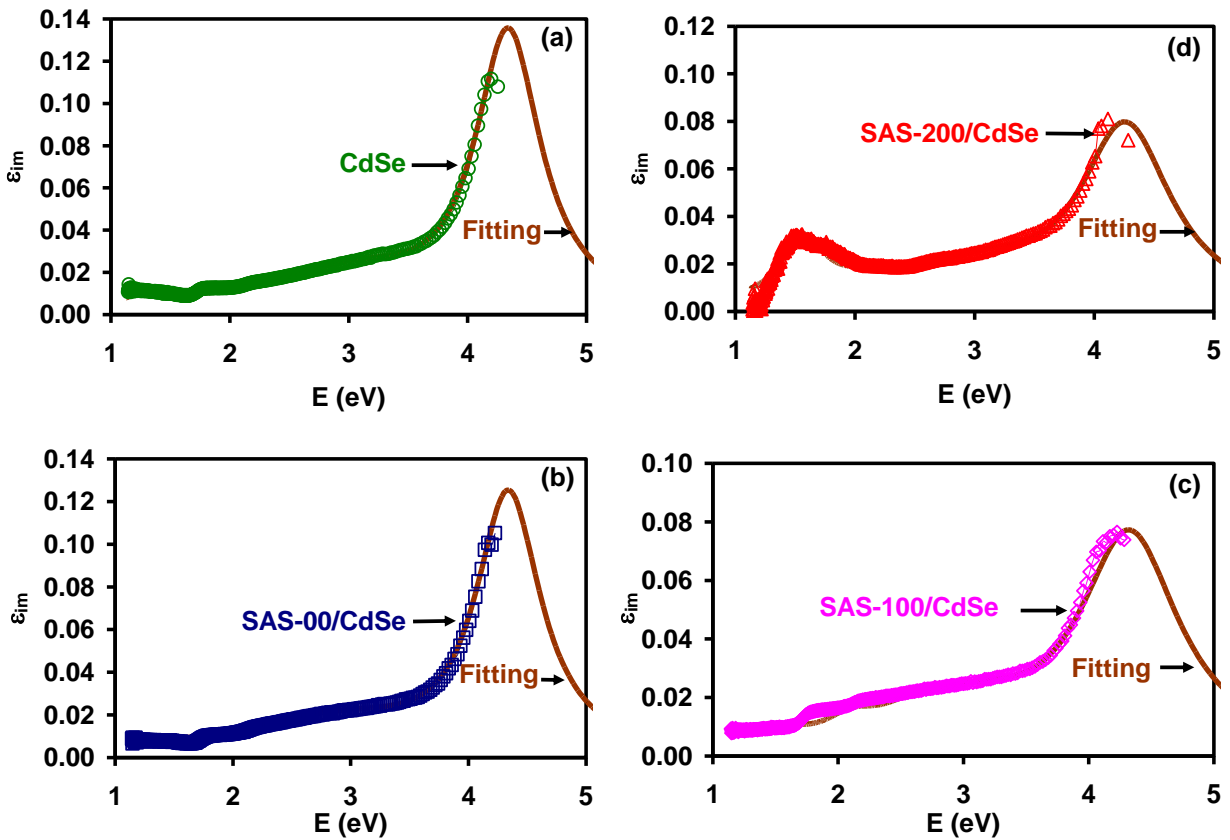


Fig. 4.14 The imaginary part of the dielectric constant spectra fitted according to the Drude-Lorentz model for (a)  $\text{CdSe}$ , (b)  $\text{SAS-00/CdSe}$ , (c)  $\text{SAS-100/CdSe}$  and (d)  $\text{SAS-200/CdSe}$ .

Table 4.5 The optical conduction parameters for (a) CdSe, (b) SAS-00/CdSe, (c) SAS-100/CdSe and SAS-200/CdSe films.

## (a) CdSe

$K_i$	1	2	3	4	5	6
$\tau$ (fs)	1.55	1.3	1.25	1.1	0.45	0.98
$p$ ( $\times 10^{17}$ cm <sup>-3</sup> )	0.7	0.7	1	0.5	20	100
$E_e$ (eV)	1.25	1.58	2.11	2.56	3.08	4.33
$\omega_p$ (GHz)	0.23	0.23	0.28	0.20	1.25	2.80
$\mu$ (cm <sup>2</sup> /Vs)	6.06	5.08	4.88	4.30	1.76	1.11

## (b) SAS-00/CdSe

$K_i$	1	2	3	4	5	6
$\tau$ (fs)	1.55	1.3	1.25	1.1	0.45	0.98
$p$ ( $\times 10^{17}$ cm <sup>-3</sup> )	0.2	0.25	0.5	0.7	6	35
$E_e$ (eV)	1.25	1.58	2.11	2.56	3.08	4.33
$\omega_p$ (GHz)	0.20	0.23	0.32	0.38	1.12	2.70
$\mu$ (cm <sup>2</sup> /Vs)	16.03	13.45	12.93	11.38	4.65	1.11

## (c) SAS-100/CdSe

$K_i$	1	2	3	4	5	6
$\tau$ (fs)	1.55	1.5	1.25	1.1	0.5	0.68
$n$ ( $\times 10^{17}$ cm <sup>-3</sup> )	0.2	0.25	0.654	0.6	5	27
$E_e$ (eV)	1.25	1.58	2.11	2.56	3.08	4.33
$\omega_p$ (GHz)	0.22	0.24	0.39	0.38	1.08	2.52
$\mu$ (cm <sup>2</sup> /Vs)	18.17	17.58	14.65	12.89	5.86	0.77

(d) SAS-200/CdSe

$K_i$	1	2	3	4	5	6
$\tau$ (fs)	0.4	1.5	0.9	0.2	0.5	0.7
$n$ ( $\times 10^{17}$ $\text{cm}^{-3}$ )	0.2	1.5	0.8	0.6	5	26.5
$E_c$ (eV)	1.25	1.58	2.11	2.56	3.08	4.27
$\omega_p$ (GHz)	0.22	0.59	0.43	0.38	1.08	2.50
$\mu$ ( $\text{cm}^2/\text{Vs}$ )	4.69	17.58	10.55	2.34	5.86	3.08

As it is readable from Table 4.5, optical oscillators are determined in three regions: infrared, visible, and ultraviolet. Each range has two oscillator  $k = 1, 2$  for the infrared region,  $k = 3, 4$  for the visible region, and  $k = 5, 6$  for the ultraviolet region. It is evident from the table that the oscillator energies of 1.25 eV, 1.58 eV, 2.11 eV, 2.56 eV, 3.08 eV and 4.33 eV are the same for all the samples for all oscillators ( $k_i=1-6$ ), respectively. In other words, SAS-XX substrates did not change the oscillator energy. This result is expected because the energy band gap was not significantly altered by SAS-XX substrates. One may think that the interaction between the SAS-XX substrates and CdSe doesn't change the electronic band structure of CdSe.

However, as seen from Table 4.5, the scattering time constant started to change as the thickness of the Au layer increased. Namely, for the ultra-violet oscillator, the scattering time constant decreases from 0.98 fs to 0.68 fs and 0.70 fs as the thickness of the Au layer increases from 0 nm to 100 nm and 200 nm, respectively. In addition, as the Au layer increases from 100 nm to 200 nm, the scattering time constant of the visible light oscillators significantly decreases.

Focusing on the drift mobility of charge carriers in the films, it is clear that the drift mobility of the carrier excited by the first oscillator ( $E_{e1} = 1.25$  eV) increased from 6.06  $\text{cm}^2/\text{Vs}$  to 16.03

$\text{cm}^2/\text{Vs}$  as a result of using the SAS-00 substrate instead of glass. Insertion of an Au layer with a thickness of 100 nm increased the mobility further. However, increasing the Au layer thickness to 200 nm reduced the drift mobility to  $4.69 \text{ cm}^2/\text{Vs}$ . This is not the same case for the second oscillator ( $E_{e2} = 1.58 \text{ eV}$ ). Namely, the drift mobility increased from  $5.08 \text{ cm}^2/\text{Vs}$  to  $13.45 \text{ cm}^2/\text{Vs}$  and reached  $17.58 \text{ cm}^2/\text{Vs}$  as the films were coated onto glass, SAS-00 and SAS-100, 200, respectively.

It is noticed from the table that the plasmon frequency tends to remain constant for all samples, regardless of the oscillator energy. An exception to this rule is observed for  $E_{e2} = 1.58 \text{ eV}$  and  $E_{e3} = 2.11 \text{ eV}$ . For these two oscillators, the plasmon frequency slightly increased with increasing Au layer thickness.

## **Chapter Five**

### **Conclusion**

Here we have employed a systematic procedure to improve the opto-electronic properties of CdSe. The procedure is based on using transparent conductive substrates to growth films. The substrates are produced by stacking two layers of SiO<sub>2</sub> and inserting Au nano sheets of thickness of 100 nm and 200 nm between them. The study here show that thicker the Au nano sheet is the more conductive the substrate, the better the crystallinity and the less the defect concentration. In addition, using SAS substrates instead of glass didn't affect the energy band gap of CdSe but formed wide band tail that narrowed upon increasing Au-layer thickness. SAS substrates enhanced the optical conductivity of CdSe. The dielectric constant value decreased in low-conductive substrates (SAS-00 and SAS-100) and increased in high-conductive substrates (SAS-200). The optical conductivity parameters also showed enhanced free carrier concentration and larger plasmon frequency values. These features indicate that the properties of CdSe have improved and become more attractive for opto-electronics.

## References

Qiu, T., Akinoglu, E. M., Luo, B., Konarova, M., Yun, J. H., Gentle, I. R., & Wang, L. (2022). Nanosphere lithography: A versatile approach to develop transparent conductive films for optoelectronic applications. *Advanced Materials*, *34*(19), 2103842.

Olusola, O. I., Echendu, O. K., & Dharmadasa, I. M. (2015). Development of CdSe thin films for application in electronic devices. *Journal of Materials Science: Materials in Electronics*, *26*, 1066-1076.

Ozmen, S. I., & Gubur, H. M. (2022). Characterization of CdSe thin film fabricated by electrodeposition. *Optoelectronics and Advanced Materials-Rapid Communications*, *16*(9-10), 453-457.

Kumar, C., Rawat, G., Kumar, H., Kumar, Y., Kumar, A., Prakash, R., & Jit, S. (2018). Electrical and ammonia gas sensing properties of PQT-12/CdSe quantum dots composite-based organic thin film transistors. *IEEE Sensors Journal*, *18*(15), 6085-6091.

Poly, L. P., Mace, B., Kottokaran, R., Bagheri, B., Noack, M., & Dalal, V. (2021, June). Novel CdSe Solar Cell. In *2021 IEEE 48th Photovoltaic Specialists Conference (PVSC)* (pp. 0443-0446). IEEE.

Patel, S. L., Chander, S., Purohit, A., Kannan, M. D., & Dhaka, M. S. (2019). Understanding the physical properties of CdCl<sub>2</sub> treated thin CdSe films for solar cell applications. *Optical Materials*, *89*, 42-47.

Garg, N. (2019). A Brief Study on Characteristics, Properties, and Applications of CdSe. In *Innovation in Materials Science and Engineering: Proceedings of ICEMIT 2017, Volume 2* (pp. 43-60). Springer Singapore.

Mustafa, M. H., Ali, H. M., Ahmed, G. S., & Hussein, B. H. (2023). Enhancement efficiency of cadmium selenium solar cell by doping within silver. *Chalcogenide Letters*, 20(10), 733-740.

Kadhim, G. A., & Mohammed, M. A. (2021, November). Influence of annealing temperature on structure and optical properties of CdSe films using radio frequency sputtering. In *AIP Conference Proceedings* (Vol. 2372, No. 1). AIP Publishing.

Al-Kotb, M. S., Al-Waheidi, J. Z., & Kotkata, M. F. (2013). Gold Schottky contacts on (0 0 2) CdSe films growing on p-type silicon wafer. *Superlattices and Microstructures*, 55, 131-143.

Zhao, J., Zeng, Y., Yang, Q., Li, Y., Cui, L., & Liu, C. (2011). VI/II ratio-dependent growth and photoluminescence of cubic CdSe epilayers by molecular beam epitaxy. *Journal of crystal growth*, 329(1), 1-5.

Ivashchenko, M. M., Kurbatov, D. I., Hnatenko, Y. P., & Opanasiuk, A. S. (2019). Luminescence study of II-VI-based thin films deposited by close-spaced vacuum sublimation technique. Nova Science.

Habte, A. G., Hone, F. G., & Dejene, F. B. (2019). The influence of malonic acid on the structural, morphological and optical properties of CdSe thin films prepared by chemical bath deposition method. *Inorganic Chemistry Communications*, 103, 107-112.

Velumani, S., Mathew, X., Sebastian, P. J., Narayandass, S. K., & Mangalaraj, D. (2003). Structural and optical properties of hot wall deposited CdSe thin films. *Solar energy materials and solar cells*, 76(3), 347-358.

Kumari, S., Chasta, G., Sharma, R., Kumari, N., & Dhaka, M. S. (2023). Phase transition correlated grain growth in CdSe thin films: Annealing evolution to cadmium chloride activation. *Physica B: Condensed Matter*, 649, 414422.

Ludescher, L., Dirin, D. N., Kovalenko, M. V., Sztucki, M., Boesecke, P., & Lechner, R. T. (2019). Impact of crystal structure and particles shape on the photoluminescence intensity of CdSe/CdS core/shell nanocrystals. *Frontiers in chemistry*, 6, 672.

Khusayfan, N. M., Qasrawi, A. F., Alharbi, S. R., Khanfar, H. K., & Kayed, T. S. (2021). Band offsets, dielectric dispersion and some applications of CdSe/GeO<sub>2</sub> heterojunctions. *Optik*, 231, 166506.

Nath, D., Singh, F., & Das, R. (2020). 120 MeV Ni<sup>10+</sup> swift heavy ions irradiation on CdSe nanocrystals induces cubic to hexagonal phase transformation-A study of microstructural modification. *Materials Science in Semiconductor Processing*, 114, 105079.

Chopade, P., Jagtap, S., & Gosavi, S. (2022). Material properties and potential applications of CdSe semiconductor nanocrystals. In *Nanoscale Compound Semiconductors and Their Optoelectronics Applications* (pp. 105-153). Woodhead Publishing.

Olusola, O. I., Echendu, O. K., & Dharmadasa, I. M. (2015). Development of CdSe thin films for application in electronic devices. *Journal of Materials Science: Materials in Electronics*, 26, 1066-1076.

Ali, A., Chiang, Y. W., & Santos, R. M. (2022). X-ray diffraction techniques for mineral characterization: A review for engineers of the fundamentals, applications, and research directions. *Minerals*, 12(2), 205.

Nguyen, T. D., Sierra, E., Eguraun, H., & Lizundia, E. (2018). Iridescent cellulose nanocrystal films: the link between structural colour and Bragg's law. *European Journal of Physics*, 39(4), 045803.

Işık, M. (2013). Optical and electrical characterization of Ga<sub>0.75</sub>In<sub>0.25</sub>Se layered single crystals.

Zubieta-Otero, L. F., Gomez-Vazquez, O. M., Correa-Piña, B. A., & Rodriguez-Garcia, M. E. (2023). Bio-inspired synthesis of bio-hydroxyapatite/synthetic hydroxyapatite hybrid nanosystems. *MedComm–Biomaterials and Applications*, 2(4), e64.

S. R. Alharbi & A. F. Qasrawi (2018). Gold and ytterbium interfacing effects on the properties of the CdSe/Yb/CdSe nanosandwiched structures. *Current Applied Physics*, 18(8), 946-951.

Qasrawi, A. F., & Omareya, O. A. (2019). In situ observations of the permanent structural modifications, phase transformations and band gap narrowing upon heating of Cu<sub>2</sub>Se/Yb/Cu<sub>2</sub>Se films. *Journal of Alloys and Compounds*, 785, 1160-1165.

Ameh, E. S. (2019). A review of basic crystallography and x-ray diffraction applications. *The international journal of advanced manufacturing technology*, 105(7), 3289-3302.

Kittel, C., & McEuen, P. (2018). *Introduction to solid state physics*. John Wiley & Sons.

Fox, M. (2002). *Optical properties of solids*. New York: Oxford University Press.

Qasrawi, A. F., & Aloushi, H. D. (2019). In situ observation of heat-assisted hexagonal-orthorhombic phase transitions in Se/Ag/Se sandwiched structures and their effects on optical properties. *Journal of Electronic Materials*, 48(12), 7906-7914.

Alharbi, S. R., & Qasrawi, A. F. (2021). Effects of Au nanoslabs on the performance of CdO thin films designed for optoelectronic applications. *Physica E: Low-dimensional Systems and Nanostructures*, 125, 114386.

Makula, P., Pacia, M., & Macyk, W. (2018). How to correctly determine the band gap energy of modified semiconductor photocatalysts based on UV-Vis spectra. *The journal of physical chemistry letters*, 9(23), 6814-6817.

Zaki, M. F. (2008). Gamma-induced modification on optical band gap of CR-39 SSNTD. *Journal of Physics D: Applied Physics*, 41(17), 175404.

Pankove, Jacques I. 2012. Optical processes in semiconductors. Courier Corporation.

He, T., Ehrhart, P., & Meuffels, P. (1996). Optical band gap and Urbach tail in Y-doped BaCeO<sub>3</sub>. *Journal of applied physics*, 79(6), 3219-3223.

Aslam, M., Kalyar, M. A., & Raza, Z. A. (2017). Graphene oxides nanosheets mediation of poly (vinyl alcohol) films in tuning their structural and opto-mechanical attributes. *Journal of Materials Science: Materials in Electronics*, 28, 13401-13413.

Alharbi, S. R., Qasrawi, A. F., & Algarni, S. E. (2021). Effects of Ag<sub>2</sub>O nanosheets on the structural, optical, and dielectric properties of GeO<sub>2</sub> stacked layers. *physica status solidi (b)*, 258(5), 2000578.

Dresselhaus, M., Dresselhaus, G., Cronin, S. B., & Souza Filho, A. G. (2018). Solid State Properties. *Alemania: Springer-Verlag*.

Hammou, B. A., El Oujdi, A., Echchelh, A., Dlimi, S., Liang, C. T., & Hemine, J. (2021). Modeling the bulk and nanometric dielectric functions of Au and Ag.

Qasrawi, A., Alharbi, S., & KJhusayfan, N. (2020). Thickness and annealing effects on the structural and optical conductivity parameters of zinc phthalocyanine thin films.

Qasrawi, A. F., & Zyoud, H. M. (2020). Optical dynamics at the Au/ZnPC interfaces. *Materials Research*, 23(3), e20200064.

Chang, W. R., Hsiao, C., Chen, Y. F., Kuo, C. F. J., & Chiu, C. W. (2022). Au nanorods on carbon-based nanomaterials as nanohybrid substrates for high-efficiency dynamic surface-enhanced Raman scattering. *ACS omega*, 7(45), 41815-41826.

Qasrawi, A. F., & Aloushi, H. D. (2019). Formation, negative capacitance and negative conductance effects in Selenium stacked layers sandwiched with Ag nanosheets. *Materials Research Express*, 6(8), 086435

Qasrawi, A. F., & Abed, T. Y. (2019). Structural and optoelectronic properties of CdS/Y/CdS thin films. *Thin Solid Films*, 679, 72-78.

AlGarni, S. E., & Qasrawi, A. F. (2022). Effects of Si slabs on the performance of CdO thin films designed for optoelectronic applications. *Materials Research*, 25, e20210622.

Qasrawi, A. F., & Shehada, S. R. (2018). Dielectric dispersion in InSe/CdS bilayers. *Physica E: Low-dimensional Systems and Nanostructures*, 103, 151-155.

Almotiri, R. A., Qasrawi, A. F., & Algarni, S. E. (2022). Ag/n-Si/p-MgSe/(Ag, C, Au, Pt) devices designed as current rectifiers, photodetectors and as AC signal filters suitable for VLC, IR and 6G technologies. *Physica Scripta*, 97(12), 125811.

Han, A., Su, H., Xu, G., Khan, M. A., & Li, H. (2020). Synthesis, crystal structures, and luminescent properties of Zn (ii), Cd (ii), Eu (iii) complexes and detection of Fe (iii) ions based on a diacylhydrazone Schiff base. *RSC advances*, 10(39), 23372-23378.

Al Harbi, S. R., & Qasrawi, A. F. (2021). Design and characterization of n-Si/p-CdO broken gap heterojunctions as high frequency PMOSFETs and microwave resonators. *IEEE Sensors Journal*, 21(12), 13223-13229.

Qasrawi, A. F., & Abu Al Rob, O. H. (2019). Enhancements of light absorbability, optical conductivity, and terahertz cutoff frequency in stacked layers of selenium via Ag nanoslabs sandwiching. *physica status solidi (a)*, 216(20), 1900370.

Ahmed, H., & Hashim, A. (2022). Tuning the Optical, Electronic and Thermal Characteristics of Si<sub>3</sub>N<sub>4</sub>/PVA/PEO Solid State Structures for Electronics Devices. *Physics and Chemistry of Solid State*, 23(1), 67-71.

Mohamed, S. H., Hadia, N. M. A., Awad, M. A., & Shaaban, E. R. (2019). Effects of thickness and Ag layer addition on the properties of ZnS thin films. *Acta Phys. Pol. A*, 135, 420-425.

Lysak, A., Przedziecka, E., Wierzbicka, A., Dłużewski, P., Sajkowski, J., Morawiec, K., & Kozanecki, A. (2022). The Influence of the Growth Temperature on the Structural Properties of {CdO/ZnO} 30 Superlattices. *Crystal Growth & Design*, 23(1), 134-141.

Qasrawi, A. F. (2018). Enhancement of photoconductive performance of CdSe via Yb nanosandwiching. *Optik*, 158, 225-230.

Al Garni, S. E., & Qasrawi, A. F. (2019). Design and characterization of MoO<sub>3</sub>/CdSe heterojunctions. *Physica E: Low-dimensional Systems and Nanostructures*, 105, 162-167.

Qasrawi, A. F. (2019). Effect of Y, Au and YAu Nano sandwiching on the structural, optical and dielectric properties of ZnSe thin films. *Chalcogenide Letters*.

Naseri, M., Hoat, D. M., Rivas-Silva, J. F., & Cocolletzi, G. H. (2020). Electronic structure, optical and thermoelectric properties of cadmium chalcogenides monolayers. *Optik*, 210, 164567.

Qasrawi, A., Abu Saa, M., Khanfar, H., & Maher, B. (2020). role of Au nanosheets in enhancing the performance of Yb/ZnS/CdS/Au tunneling photosensors.

Hashmi, G., Basher, M. K., Hoq, M., & Rahman, M. H. (2018). Band gap Measurement of P-type Monocrystalline Silicon Wafer. *Bangladesh Journal of Scientific and Industrial Research*, 53(3), 179-184.

Wu, S., Tan, N., Lan, D., & Yi, B. (2018). Photoinduced Synthesis of Hierarchical Flower-Like Ag/Bi<sub>2</sub>WO<sub>6</sub> Microspheres as an Efficient Visible Light Photocatalyst. *International Journal of Photoenergy*, 2018(1), 8138064

Qasrawi, A., & Abu Ghannam, A. (2022). Effect of transparent Pb substrates on the structural, optical, dielectric and electrical properties of copper selenide thin films.

Rahman, M. F., Melody, Z. R., Ali, M. H., Ghosh, A., Barman, P., Islam, M. R., & Hossain, M. K. (2023). First-principles analysis of how Cobalt doping affects the structural, electronic, and optical properties of  $\alpha$ -MoO<sub>3</sub>. *Indian Journal of Physics*, 1-10.

Dey, A., Sharma, R., & Dar, S. A. (2020). An extensive investigation of structural, electronic, thermoelectric and optical properties of bi-based half-Huesler alloys by first principles calculations. *Materials Today Communications*, 25, 101647.

Chanana, R. K. (2023). Discussion on the Electron and Hole Effective Masses in Thermal Silicon Dioxide. *Journal of Materials Science and Engineering A*, 13(4-6), 30-34.

Qasrawi, A. F., & Hamarsheh, A. A. (2021). Au/CdBr<sub>2</sub>/SiO<sub>2</sub>/Au Straddling-Type Heterojunctions Designed as Microwave Multiband Pass Filters, Negative Capacitance Transistors, and Current Rectifiers. *physica status solidi (a)*, 218(22), 2100327.

Qasrawi, A. F. (2019). Effect of Y, Au and YAu nanosandwiching on the structural, optical and dielectric properties of ZnSe thin films.

## الملخص

في هذه الأطروحة، هدفتنا إلى تحسين الخصائص البصرية للأفلام الرقيقة من CdSe عن طريق طليها على ركائز SiO<sub>2</sub> عالية التوصيل. تم ترسيب الأفلام الرقيقة من CdSe باستخدام تقنيات التبخير الحراري على ركائز SiO<sub>2</sub> الموصلة تحت ضغط فراغي قدره 10<sup>-4</sup> ملي بار. تم استخدام طبقات مكدسة من أفلام SiO<sub>2</sub> تحتوي على صفائح نانوية من الذهب (SAS). لوحظ أن ركائز SiO<sub>2</sub> التي تحتوي على صفائح نانوية من الذهب في بنيتها أثرت بشكل كبير على الخصائص الهيكلية والبصرية لـ CdSe. تحديداً، تناقصت المعلمات الشبكية لخلية الوحدة السداسية لـ CdSe السداسية عند استبدال الزجاج بركائز SAS. بالإضافة إلى ذلك، انخفض كل من الإجهاد الدقيق ونسبة العيوب والتكدس، مما يشير إلى تحسين تبلورية الأفلام باستخدام ركائز SAS. علاوة على ذلك، لوحظ أن أفلام SAS لا تلعب دوراً كبيراً في فجوة الطاقة ولكنها تشكل ذيولاً للطاقة داخل الفجوة. تضاءلت حالات الذيل الأسيّة مع زيادة سمك طبقة الذهب. من ناحية أخرى، أظهرت تحليلات تشتت العازل أن أطيف الثابت العازل تحددت بواسطة ثلاثة مذبذبات والتي تحركت نحو الأزرق عند استبدال الزجاج بركائز SAS. انخفضت قيم الثابت العازل مع زيادة سمك طبقة الذهب في الركيزة بسبب زيادة كثافة الشحنة الحرة الناتجة عن طبقة الذهب السميكة. علاوة على ذلك، أظهرت أطيف التوصيلية البصرية، التي تم نمذجتها باستخدام نهج درود-لورنتز، ميزات مثيرة للاهتمام. على وجه الخصوص، زادت التوصيلية البصرية لـ CdSe وزادت كثافة الشاحنات الحرة بعد استخدام ركائز SAS. هذه الخصائص تجعل الأفلام مناسبة للتطبيقات الضوئية الإلكترونية.